

# Two-dimensional transition-metal dichalcogenides-based bilayer heterojunctions for efficient solar cells and photocatalytic applications

Khushboo Dange,<sup>\*</sup> Rachana Yogi,<sup>†</sup> and Alok Shukla<sup>‡</sup>

*Department of Physics, Indian Institute of Technology Bombay, Powai, Mumbai 400076, India*

In this work, we present a first-principles investigation of the optoelectronic properties of vertically-stacked bilayer heterostructures composed of 2D transition-metal dichalcogenides (TMDs). The calculations are performed using the density-functional theory (DFT) as well as many-body perturbation theory within  $G_0W_0$ -BSE methodology. Our aim is to propose these TMD heterostructures for potential applications in solar cells. The TMD monolayers comprising the heterojunctions considered in this research are  $\text{MoS}_2$ ,  $\text{WS}_2$ ,  $\text{MoSe}_2$ , and  $\text{WSe}_2$  due to their favorable band gaps, high carrier mobility, robust absorption in the visible region, and excellent stability. These four TMD monolayers provide the basis for a total of six potential heterostructures. Consequently, we have examined the structural, electronic, and optical properties of six heterostructures ( $\text{WS}_2/\text{MoS}_2$ ,  $\text{MoSe}_2/\text{MoS}_2$ ,  $\text{MoSe}_2/\text{WS}_2$ ,  $\text{WSe}_2/\text{MoS}_2$ ,  $\text{WSe}_2/\text{MoSe}_2$ , and  $\text{WSe}_2/\text{WS}_2$ ). At the DFT level, all the six considered TMD heterostructures meet the essential criterion of type II band alignment, a critical factor in extending carrier lifetime. However, according to  $G_0W_0$  results,  $\text{MoSe}_2/\text{WS}_2$  does not exhibit the type II band alignment, instead it shows type I band alignment. The significantly large quasi particle gaps obtained from  $G_0W_0$  approximation suggest the presence of strong electron-correlation effects. The chosen heterostructures exhibit superior optoelectronic properties compared to their respective isolated monolayers. The quite significant values of the intrinsic electric fields which arise due to the asymmetric geometry of the heterostructures are obtained. Additionally, the obtained small and nearly equal electron and hole effective masses indicate high mobility and efficient charge carrier separation, resulting in low recombination losses. The quality of these heterojunction solar cells is estimated by computing their power conversion efficiencies (PCE). The PCEs are calculated at both the HSE06 and  $G_0W_0$  levels,

and the maximum PCE predicted by HSE06 calculations on our designed solar cells can reach up to 19.25% for the  $\text{WSe}_2/\text{WS}_2$  heterojunction. In addition, all the six TMD heterostructures are examined for their potential applications in photocatalysis for hydrogen evolution reaction, and the three of them, namely,  $\text{WS}_2/\text{MoS}_2$ ,  $\text{MoSe}_2/\text{MoS}_2$ , and  $\text{WSe}_2/\text{MoS}_2$  heterostructures qualify for the same.

**Keywords:** Transition-metal dichalcogenides; vertical heterostructures; solar cells; density functional theory;  $G_0W_0$ -BSE; optoelectronic properties; power conversion efficiency; photocatalysis

## I. INTRODUCTION

As traditional fossil fuel-based sources are proving to be unsustainable and detrimental to the environment, non-conventional energy resources are emerging as viable alternatives. Solar energy is one such non-conventional energy resource, which provides a clean, renewable, and abundant alternative [1]. The electricity can be generated by harnessing the power of the sun without emitting harmful greenhouse gases, thereby reducing our carbon footprint and mitigating climate change. With advancing technology and decreasing costs, the use of solar energy can drive economic growth and empower communities to become self-sufficient in meeting their energy needs. However, designing devices for harvesting solar power on a large scale in a commercially viable manner continues to be a big challenge for scientists [2]. 2D materials have opened up exciting possibilities for enhancing efficiency of harvesting solar energy. These ultrathin materials such as graphene [3], transition metal dichalcogenides (TMDs) [4, 5], and perovskites [6], possess desirable optoelectronic properties, making them highly suitable for solar cell applications. Their large surface area and excellent electrical conductivity [7, 8] allow for efficient charge separation, resulting in improved performance. Moreover, 2D materials can be engineered to absorb light across a broad spectrum, enabling them to capture a wider range of solar radiations. With the advancement of novel 2D materials, their heterojunctions held together by van der Waals (vdW) interactions have been demonstrated both theoretically and practically, not just to probe the fundamental

---

\* khushboodange@gmail.com

† yogirachana04@gmail.com

‡ shukla@iitb.ac.in

physics, but also for their potential device applications [9, 10]. The weak vdW interlayer forces not only retain several desirable intrinsic properties of the stacked structures, but also result in new ones such as the increased optical absorption range [11], charge transfer [12], band alignment [13], etc. Heterojunctions with type II band alignment play a significant role in increasing solar energy harvesting efficiency. The presence of a type-II band alignment in a heterostructure comprising two semiconductors, with one serving as a donor and the other one as an acceptor, results in the segregation of photoexcited electrons and holes at the interface. This results in an indirect exciton formation, which thereby reduces the carrier recombination rate.

Among the 2D material family, TMDs are emerging as promising candidates for applications in catalysis, energy storage, gas sensing, field-effect transistors, logic circuits, and optoelectronics particularly due to their semiconducting characteristics, strong chemical stability, and flexibility [14–18]. Bulk TMDs formed by transition metals ( $M = \text{Mo}, \text{W}$ ) and chalcogens ( $X = \text{S}, \text{Se}$ ) exist in two structural phases i.e., trigonal prismatic (2H) and octahedral (1T) phases depending on the different stacking order of the three atomic planes (X-M-X) [8]. Both the 2H and 1T phases are thermodynamically stable. The synthesis of monolayer TMDs has already been reported in various studies [19–22]. These TMDs undergo indirect to direct band gap transition on reducing the thickness from bulk to monolayer [23, 24]. The direct band gap in the visible region of the spectrum, high carrier mobility, exotic optical properties, and high stability in ambient conditions make these TMD monolayers potential candidates to be used in heterojunction solar cells [25]. Several heterojunction solar cell devices composed of other 2D materials with TMDs have been proposed theoretically or realized experimentally, such as graphene/MoS<sub>2</sub> [26], phosphorene/MoS<sub>2</sub> [27], MoSe<sub>2</sub>/ψ-phosphorene [28], and tellurene/MX<sub>2</sub> ( $M=\text{Mo}, \text{W}$ ;  $X=\text{S}, \text{Se}, \text{Te}$ ) [29]. Heterostructures in which both the considered 2D materials are TMDs have also been investigated both experimentally and theoretically [30–33]. Kim *et al.* [30] investigated the sensing properties of the WSe<sub>2</sub>/WS<sub>2</sub> and MoS<sub>2</sub>/WSe<sub>2</sub> heterojunctions for NO<sub>2</sub> and NH<sub>3</sub> gases. Their study confirmed that 2D TMD heterostructures possess potential for use in gas sensor applications without external biasing. Chen *et al.* [31] synthesized some 2D TMD heterostructures on Si/SiO<sub>2</sub> substrates and explored their Raman and photoluminescence spectra. The successful synthesis of various 2D TMD heterostructures using controllable interfaces provides exciting opportunities to design a variety of novel optoelectronic devices. Amin *et al.* [32]

studied the electronic and optical properties of out-of-plane and in-plane heterostructures of 2D TMDs and predicted their potential for photocatalytic applications.

The present study employs first-principles density-functional theory calculations augmented by the inclusion of the electron-correlation effects within a  $G_0W_0$ -BSE approach to study the TMD vertical heterostructures for their possible applications in solar cells. By considering all possible combinations, in total six heterostructures are formed using the 1H phases of four TMDs monolayers ( $MX_2$ , where  $M = \text{Mo, W}$ ;  $X = \text{S, Se}$ ). The electronic and optical properties of all the heterostructures are investigated in detail, along with the calculation of their power conversion efficiencies. All the six considered heterostructures exhibit type II band alignment at the HSE06 level, whereas, at the  $G_0W_0$  level,  $\text{MoSe}_2/\text{WS}_2$  heterostructure displays a type I band alignment, while the rest still have a type II band alignment. After thoroughly examining the properties relevant for photovoltaics, we delve into a study of the photocatalytic performance of all the six considered TMD heterostructures. To the best of our knowledge, a comparative study of this type both at the HSE06, as well as  $G_0W_0$ -BSE levels, has not been reported so far.

The remainder of this paper is organized in the following manner. The next section contains the details of the employed computational tools in brief, followed by a systematic presentation and discussion of our results in Sec. III. Finally, we conclude by summarizing our findings in Sec. IV.

## II. COMPUTATIONAL METHODS

Our calculations were performed using the plane-wave based Vienna ab initio simulation package (VASP) [34, 35] which employs a first-principles based density functional theory (DFT) [36, 37]. Further, Perdew-Burke-Ernzerhof (PBE) [38] exchange correlation functional of the generalized gradient approximation (GGA) is used in all the calculations. The electronic structure calculations are also performed using the Heyd-Scuseria-Ernzerhof (HSE06) [39] hybrid functional to overcome the band gap under estimation by the GGA functionals. Since both these functionals do not correctly describe the vdW interactions, we adopted the non-local optB88-vdW [40] dispersion corrections to account for them in the considered heterostructures. The projected augmented wave (PAW) [41, 42] method is used, which includes pseudopotentials coupled with the plane wave basis set. In these

calculations, we used a relatively large basis set with the kinetic energy cutoff of 600 eV. Our calculations were performed on the primitive cells so that the monolayer calculations involved three atoms, while the heterostructure calculations were performed using six atoms. The vacuum of 20 Å and 25 Å are created along the  $z$ -direction in the case of monolayers and heterostructures, respectively, to avoid the interaction with their periodic copies. The geometries are optimized until the Hellman-Feynman force acting on each atom is less than 0.01 eV/Å, while the convergence criterion for the self-consistent-field (SCF) iterations was  $10^{-5}$  eV on the total energy of the system. The Brillouin zone integration is performed using the Monkhorst-Pack  $k$ -points grid [43], and meshes of the sizes  $9 \times 9 \times 1$  and  $9 \times 9 \times 2$  are employed for the geometry optimization of the TMD monolayers and heterostructures, respectively. Next, the refined  $k$ -mesh of  $12 \times 12 \times 1$  is used for further calculations on the optimized monolayers, but in case of heterojunctions, the  $k$ -mesh is not refined due to the high computational cost. The effect of spin-orbit coupling (SOC) is also taken into consideration in both the GGA-PBE and HSE06 calculations on the optimized structures as it is significant for both the Mo and W atoms. Despite the fact that the TMD monolayers under consideration are non-magnetic in nature, effect of spin-polarization is taken into account during the optimization of the heterostructures, which verifies their non-magnetic nature. Following this, all the calculations are performed under a non-spin-polarized condition.

To calculate the quasiparticle (QP) energies, we employed the many-body perturbation theory using the GW approximation [44]. Specifically, we performed single-shot  $G_0W_0$  calculations based on the Bloch functions obtained from the GGA-PBE calculations, and a kinetic-energy cutoff of 400 eV for the response function was employed. We included 160 unoccupied bands for the  $G_0W_0$  calculations which are further increased to 200 to check the convergence of our results. Notably, the QP band gap values obtained with 200 unoccupied bands were nearly identical to those with 160 bands. As a result, we proceeded with 160 unoccupied bands for further calculations. To obtain the  $G_0W_0$  band structures, we used the Wannier interpolation approach, as implemented in Wannier90 program [45]. For the Wannier interpolation, the initial projections were chosen as the  $d$  orbitals of transition metals (Mo, W) and  $p$  orbitals of chalcogens (S, Se). The band alignment at the  $G_0W_0$  level is obtained using the band-gap center as a reference, as it has been shown to be relatively insensitive to the choice of functional [46]. According to the method proposed by Toroker *et al.* [47], QP band edges were determined as

$$E_{CBM/VBM} = E_{BGC} \pm \frac{1}{2}E_g^{QP}, \quad (1)$$

where  $E_g^{QP}$  denotes the  $G_0W_0$  band gap,  $E_{BGC}$  is the band-gap center, and  $E_{CBM}$  and  $E_{VBM}$ , respectively, denote the positions of the valence band maximum (VBM) and conduction band minimum (CBM) with respect to the vacuum, respectively.

For the calculation of the optical absorption spectra, we solve the Bethe-Salpeter equation (BSE) [48, 49]

$$(E_{c\mathbf{k}} - E_{v\mathbf{k}})A_{vc\mathbf{k}}^S + \sum_{\mathbf{k}'\mathbf{v}'\mathbf{c}'} \langle v\mathbf{c}\mathbf{k} | K_{eh} | v'\mathbf{c}'\mathbf{k}' \rangle A_{v'\mathbf{c}'\mathbf{k}'}^S = \Omega^S A_{vc\mathbf{k}}^S \quad (2)$$

where  $E_{v\mathbf{k}}$  and  $E_{c\mathbf{k}}$  are the QP energies of the valence and conduction band states, respectively,  $A_{vc\mathbf{k}}^S$  is the electron-hole amplitude matrix corresponding to transition S,  $\Omega^S$  represents the eigenenergies corresponding to the transition, while  $K_{eh}$  is the interaction kernel. Eq. 2 are solved within the Tamm-Dancoff approximation[50], using the single-particle states obtained from the  $G_0W_0$  calculations. We found that the four topmost valence bands and four lowest conduction bands as the basis for the excitonic states in the Bethe-Salpeter kernel ( $K_{eh}$ ) are sufficient for the relatively low-energy optical excitations that we are interested in.

### III. RESULTS AND DISCUSSION

#### A. Electronic structure of TMD Monolayers

We first considered TMD monolayers ( $\text{MoS}_2$ ,  $\text{MoSe}_2$ ,  $\text{WS}_2$ , and  $\text{WSe}_2$ ) in their 1H phase, and calculated their electronic properties using the optimized structures. A monolayer of these TMDs consists of three atomic planes, out of which one layer of metal atoms (M) is sandwiched between two layers of chalcogens (X). These monolayers have  $P6m2$  space group with the  $D_{3h}$  point group symmetry, and their optimized geometries are shown in Fig. 1, with the optimized lattice constants reported in Table I. The obtained lattice constant for each of the monolayers is consistent with the values reported in literature [29, 51, 52]. The electronic band structures are obtained using both the PBE and HSE06 functionals, and the corresponding band gap ( $E_g$ ) values are presented in Table I. The calculated HSE06 band structures of the considered monolayers are presented in Figs. S1(a)-(d) of the Supplemental

Material (SM). For each of the four monolayers, a direct band gap is obtained at K-point using both the functionals. The band gap values and their direct nature are consistent with the previously reported results [29, 53]. The obtained upward splittings in VBM due to SOC are 0.15 eV, 0.43 eV, 0.19 eV, and 0.47 eV for the  $\text{MoS}_2$ ,  $\text{WS}_2$ ,  $\text{MoSe}_2$ , and  $\text{WSe}_2$  monolayers, respectively, in agreement with the literature [54]. The  $E_g$  values obtained using the HSE06 functional are close to the experimentally reported values mentioned in Table I. The direct band gap is an important factor for better optoelectronic properties. For highly efficient heterojunction solar cells, both donor and acceptor semiconductors should possess a desirable band gap, i.e., in the range of 1.10 eV–1.74 eV [55], so as to guarantee a wide sunlight absorption range. Thus, based on the band gap criterion,  $\text{MoSe}_2$  and  $\text{WSe}_2$  are relatively better candidates for heterojunction solar cells. Further, the considered monolayers can achieve high carrier mobility (values are presented in Table S1 of the SM), resulting in efficient carrier transport [56, 57].

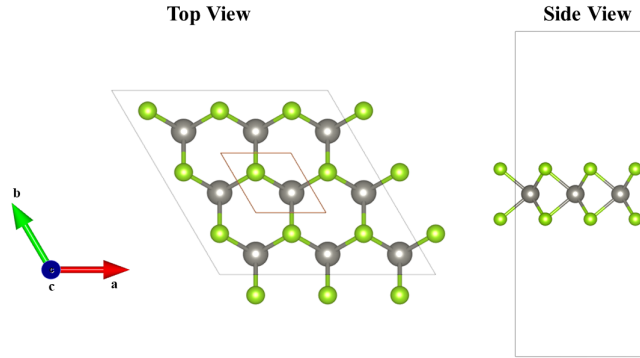


Figure 1. Structure of the considered TMD monolayers. Here, grey and green spheres represent the M (=Mo or W) and X (=S or Se) atoms, respectively.

Table I. Calculated lattice constants and the electronic band gaps for the considered TMD monolayers.

S.No. Monolayers		Lattice Constant (Å)	Band Gap (eV)				
			PBE	HSE06	$G_0W_0$	$G_0W_0 + \text{SOC}$	Experimental
1	MoS <sub>2</sub>	3.180	1.59 [53]	2.02[53]	2.50	2.42	1.90 [23, 58]
2	WS <sub>2</sub>	3.190	1.51 [53]	1.96[53]	2.76	2.50	1.96 [59], 2.0 [60]
3	MoSe <sub>2</sub>	3.320	1.32 [29]	1.71[29]	2.17	2.06	1.58 [61]
4	WSe <sub>2</sub>	3.319	1.24 [29]	1.65[29]	2.70	2.40	1.96 [62]

The  $G_0W_0$  band structures are also calculated for the considered TMD monolayers. We first calculated the Wannier-interpolated PBE band structures (without SOC) and compared them to the DFT band structures, as shown in Fig. S2 of the SM for the MoS<sub>2</sub> monolayer. After confirming that the Wannierized band structures closely matched the DFT results, we proceeded to calculate the  $G_0W_0$  band structures using the same set of Wannier functions. The resultant  $G_0W_0$  band structures of all the four monolayers are presented in Figs. S1(e)-(h) of the SM. The corresponding QP band gaps ( $E_g^{QP}$ ) obtained from the  $G_0W_0$  approximation are listed in Table I. These band gaps, significantly larger than those obtained from HSE06 calculations, suggest the presence of strong electron-correlation effects, and are consistent with the previously reported values [54, 63]. For example, our  $E_g^{QP}$  values for MoS<sub>2</sub> (2.50 eV) and MoSe<sub>2</sub> (2.17 eV) monolayers are in excellent agreement with the values reported by Torun *et al.* (2.54 eV and 2.19 eV, respectively) [64]. Further,  $G_0W_0$  approximation does not alter the nature of the band gaps, as a direct band gap (at K) persists for all the four monolayers. Since the effect of SOC is not included in the  $G_0W_0$  gaps, we obtained SOC corrected  $G_0W_0$  gaps by rigidly shifting the CBM and VBM by the same amount as the corresponding shifts observed in the PBE band structures computed including the SOC, and the results are reported in Table I. Notably, our SOC-corrected  $E_g^{QP}$  for the MoS<sub>2</sub> monolayer (2.42 eV) closely matches the gap reported by Alejandro *et al.* [63] (2.41 eV) who included SOC in the SCF calculations, thus validating our approach of applying a rigid shift to account for SOC in the  $G_0W_0$  gaps. Given that PBE underestimates the band gap, we continued with the HSE06 and  $G_0W_0$  results to assess the band alignment between the



monolayers in the heterostructures under consideration, as well as to study their potential for solar cell applications.

### B. Optical spectra of TMD monolayers

The BSE calculations are performed to obtain the optical response of the considered monolayers. Both the imaginary and real parts of dielectric function ( $\epsilon(\omega)$ ), defined as  $\epsilon(\omega) = \epsilon_{Re}(\omega) + i\epsilon_{Im}(\omega)$  are obtained by performing the BSE simulations. The imaginary part of dielectric function ( $\epsilon_{Im}(\omega)$ ) describes the optical absorption properties and is presented in Fig. S3 of the SM for all the monolayers. It is observed that the first peak occurs at an energy lower than the QP gap obtained using the  $G_0W_0$  approximation. This suggests that the optical gap,  $E_g^{op}$ , is smaller than the electronic gap due to excitonic effects caused by electron-hole attraction. The  $E_g^{op}$  values obtained from the BSE spectrum (Fig. S3 of the SM) and the corresponding exciton binding energies,  $E_{ex}$ , calculated as  $E_{ex} = E_g^{QP} - E_g^{op}$  are tabulated below (see Table II). Further, the SOC corrected optical gaps, listed in the same table (see Table II) are obtained by subtracting  $(E_g)_{G_0W_0} - (E_g)_{G_0W_0+SOC}$  from the original  $E_g^{op}$  values, which did not account for SOC. The SOC corrected  $E_g^{op}$  values thus obtained show excellent agreement with the experimental gaps (see Table I), further validating our approach of accounting for SOC through a rigid shift. Moreover, the obtained  $E_{ex} \sim 0.5$  eV for all the four TMD monolayers agree well with both the theoretical [65] and experimental studies [66, 67]. The larger  $E_{ex}$  values observed for the W based TMD monolayers are consistent with the stronger electron correlation effects arising from the contribution of  $4f$  and  $5d$  electrons, as compared to just  $4d$  electrons in the Mo based TMD monolayers.

Table II. Optical gaps,  $E_g^{op}$  obtained from the BSE calculations and the corresponding exciton binding energies,  $E_{ex}$  for the considered TMD monolayers.

S.No.	Monolayers	$E_g^{op}$ (eV)		$E_{ex}$ (eV)
		BSE	BSE+SOC	
1	MoS <sub>2</sub>	2.04	1.96	0.46
2	WS <sub>2</sub>	2.27	2.01	0.49
3	MoSe <sub>2</sub>	1.71	1.60	0.46
4	WSe <sub>2</sub>	2.17	1.87	0.53

### C. Selection Criteria for heterostructures formation

Total six combinations of two different semiconductors are possible using the four considered TMD monolayers. When assessing the potential of two materials for heterostructure formation, their lattice constants play a crucial role. The lattice mismatch ( $\nu$ ) between the two semiconductors can be calculated using the following formula:

$$\nu = \frac{2|a_1 - a_2|}{a_1 + a_2} \times 100\%, \quad (3)$$

where  $a_1$  and  $a_2$  are the lattice constants of the semiconductors involved in the formation of heterostructure. Using Eq. 3 and the obtained lattice constants for the monolayers (Table I), we have calculated  $\nu$  for the six possible heterostructures (see Table III). Relatively small values of  $\nu$  ( $< 5\%$ ) obtained for all the six combinations, combined with the fact that all the monolayers have the same geometric symmetries suggests that it is possible to make vertically-stacked bilayer heterojunctions from them. As a result of lattice mismatch, the two layers get strained during optimization.

Table III. Calculated lattice mismatch ( $\nu$ ) for the TMD heterostructures under consideration.

Heterostructures	WS <sub>2</sub> /MoS <sub>2</sub>	MoSe <sub>2</sub> /MoS <sub>2</sub>	MoSe <sub>2</sub> /WS <sub>2</sub>	WSe <sub>2</sub> /MoS <sub>2</sub>	WSe <sub>2</sub> /MoSe <sub>2</sub>	WSe <sub>2</sub> /WS <sub>2</sub>
$\nu$ (%)	0.30	4.30	3.99	4.27	0.03	3.96

Another important factor is that the type II band alignment, shown in Fig. 2(a), between

the two chosen semiconductors for a heterostructure is crucial for its application in solar cells. This is because in type II band alignment, the photoexcited electrons generated in a semiconductor (donor) are confined to one side (lowest conduction band of the acceptor) of the heterostructure, and holes are confined to the other side (highest occupied valence band of the donor). This spatial separation of electrons and holes results in an indirect exciton formation and thus reduces carrier recombination losses, leading to longer carrier lifetimes and improved overall efficiency. To determine the type of band alignment, band edge positions,  $E_{CBM}$  and  $E_{VBM}$  of the considered TMD monolayers are calculated using the results of both the HSE06 functional and  $G_0W_0$  approximation. In case of  $G_0W_0$  calculations, the band edge positions are computed using Eq. 1, and the calculated  $E_{CBM}$  and  $E_{VBM}$  at the HSE06 and  $G_0W_0$ (without and with SOC) levels are summarized in Table IV, as well as shown in an energy level diagram in Fig. 2(b). It is found that the five heterostructures,  $\text{MoSe}_2/\text{MoS}_2$ ,  $\text{WS}_2/\text{MoS}_2$ ,  $\text{WSe}_2/\text{MoS}_2$ ,  $\text{WSe}_2/\text{MoSe}_2$ , and  $\text{WS}_2/\text{WSe}_2$ , exhibit type II band alignment according to both the HSE06 calculations and  $G_0W_0$  approximation, in agreement with the literature [54]. However, for  $\text{MoSe}_2/\text{WS}_2$ , HSE06 calculations predicts type II alignment, whereas,  $G_0W_0$  (both with and without SOC) indicates type I alignment. This discrepancy in band alignment between  $\text{MoSe}_2$  and  $\text{WS}_2$  monolayers has also been reported in previous theoretical and experimental studies [54, 68, 69]. The convention A/B is used throughout the paper, to represent the considered heterostructures, in which A and B denote the semiconductors acting as donor and acceptor, respectively.

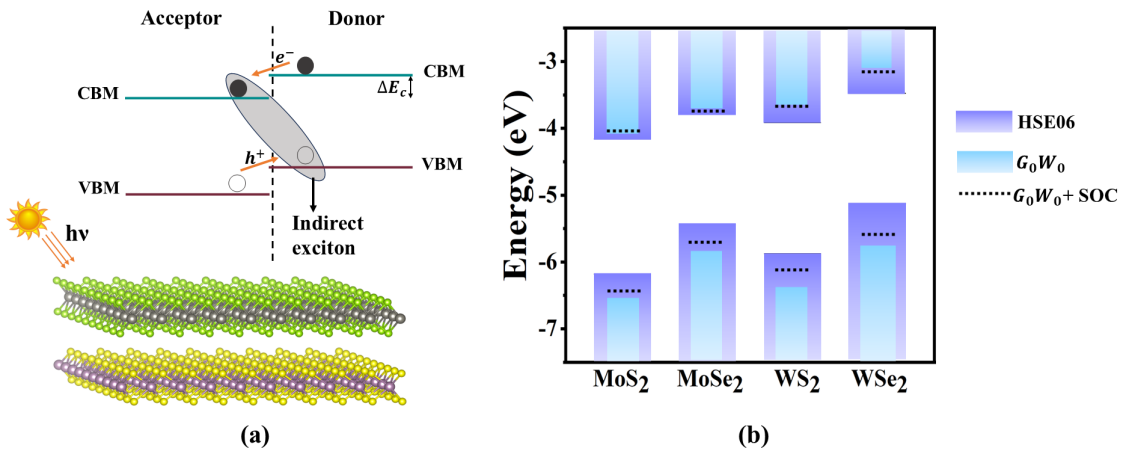


Figure 2. (a) Schematics of the type II band alignment and (b) Position of the VBM and CBM energy levels of the considered TMD monolayers with respect to vacuum under different approaches.

Table IV. Band edge positions,  $E_{VBM}$  and  $E_{CBM}$  of the considered TMD monolayers with respect to vacuum, computed at the HSE06,  $G_0W_0$ , and  $G_0W_0 + \text{SOC}$  level.

Monolayers	$E_{VBM}(\text{eV})$				$E_{CBM}(\text{eV})$			
	HSE06	$G_0W_0$	$G_0W_0 + \text{SOC}$		HSE06	$G_0W_0$	$G_0W_0 + \text{SOC}$	
MoS <sub>2</sub>	-6.181	-6.559	-6.481		-4.159	-4.060	-4.059	
WS <sub>2</sub>	-5.877	-6.391	-6.166		-3.914	-3.627	-3.665	
MoSe <sub>2</sub>	-5.448	-5.846	-5.745		-3.739	-3.678	-3.681	
WSe <sub>2</sub>	-5.127	-5.801	-5.544		-3.475	-3.097	-3.140	

#### D. Calculated properties of TMD heterostructures

##### 1. Structural Properties

The vertical heterostructures formed using TMD monolayers are shown in Fig. 3. To form these heterostructures, the AA' type of stacking is considered, in which two layers are aligned antiparallel to each other and an X atom of the lower layer lies below a M atom of the top layer. The lattice constants ( $a$ ) of the optimized heterostructures are presented in Table V, and on comparing these lattice constants with those of the constituent monolayers, we found that the monolayers get strained to attain the ground state. For instance, from the lattice constant of MoSe<sub>2</sub>/MoS<sub>2</sub> (3.18 Å), we infer that MoSe<sub>2</sub> layer gets compressed, while the MoS<sub>2</sub> layer remains unstrained. The optimized interlayer distance  $d$ , i.e., the perpendicular distance between the M-atom layers of the two monolayers, is obtained in the range of 6.0 Å – 6.3 Å for all the considered heterostructures (see Table V for exact values), close to the reported values [64, 70]. To determine the stability of these heterostructures, their formation energies ( $E_f$ ) are calculated using the following formula

$$E_f = E_{hetero} - (E_{layer1} + E_{layer2}) \quad (4)$$

where  $E_{hetero}$  represents the total energy of the heterostructure, while  $E_{layer1}$  and  $E_{layer2}$  denote the energies of the two different TMD monolayers constituting the heterojunction. The calculated  $E_f$  values are presented in Table V. The negative  $E_f$  values are obtained for all

the six heterostructures in the range -0.31 eV to -0.39 eV, confirming their stability. Further, the weak vdW interactions between the two constituent layers of the heterostructures are responsible for the small  $E_f$  values.

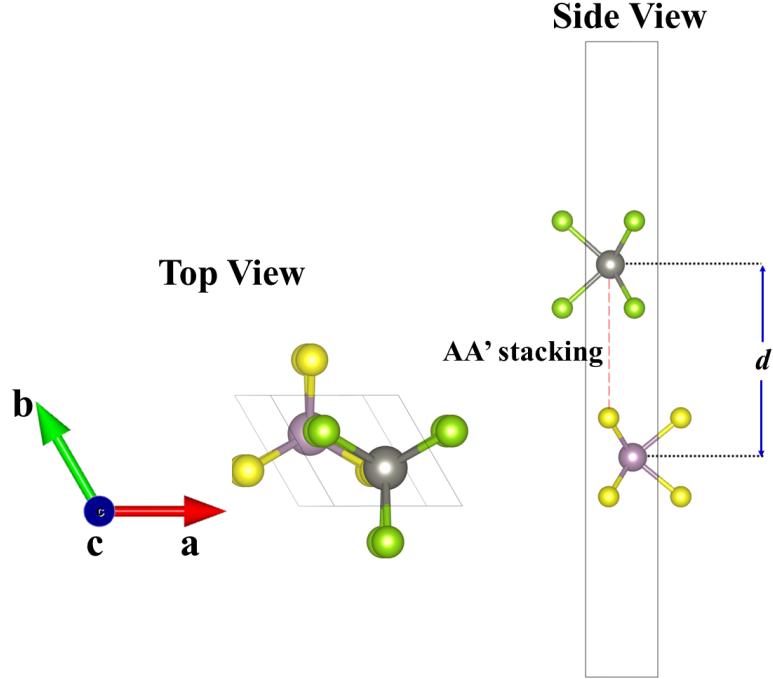


Figure 3. The vertical heterostructures of TMDs, formed using AA' stacking. Here, purple and grey spheres symbolize the metal atoms M (= Mo or W), while yellow and green spheres stand for the chalcogen atoms X (=S or Se), of the two different layers.

Table V. Calculated interlayer distances ( $d$ ), lattice constants ( $a$ ), and formation energies ( $E_f$ ) for the TMD heterostructures under consideration.

S.No.	Heterostructures	$d$ (Å)	$a$ (Å)	$E_f$ (eV)
1	WS <sub>2</sub> /MoS <sub>2</sub>	6.00	3.12	-0.36
2	MoSe <sub>2</sub> /MoS <sub>2</sub>	6.11	3.18	-0.32
3	MoSe <sub>2</sub> /WS <sub>2</sub>	6.14	3.18	-0.31
4	WSe <sub>2</sub> /MoS <sub>2</sub>	6.13	3.18	-0.31
5	WSe <sub>2</sub> /MoSe <sub>2</sub>	6.30	3.24	-0.39
6	WSe <sub>2</sub> /WS <sub>2</sub>	6.14	3.18	-0.31

Furthermore, ab-initio molecular dynamics (AIMD) [71] simulations have also been performed to explore the stability of the considered heterostructures. These simulations were performed on larger sized  $2 \times 2$  supercells of the considered heterostructures, as compared to the DFT calculations that were done on the primitive cells. The AIMD calculations were carried out in canonical ensemble utilizing the Nose-Hoover thermostat [72] at 500K for a total duration of 5000 fs in the steps of 1 fs. The resultant total energy as a function of time steps is depicted in Fig. 4 for the MoSe<sub>2</sub>/MoS<sub>2</sub> and WSe<sub>2</sub>/WS<sub>2</sub> systems, while for the rest of the heterostructures, they are shown in Fig. S4 of the SM. The plotted graphs showed minimal variations in the total energies, which confirms the stability of the considered heterostructures at higher temperatures as well. The corresponding structures obtained during the AIMD simulations are also shown in the inset. The maximum average changes in the Mo-S, Mo-Se, W-S, and W-Se bond lengths during the course of the simulations are 0.06 Å, 0.05 Å, 0.06 Å, and 0.03 Å, respectively, which are quite small.

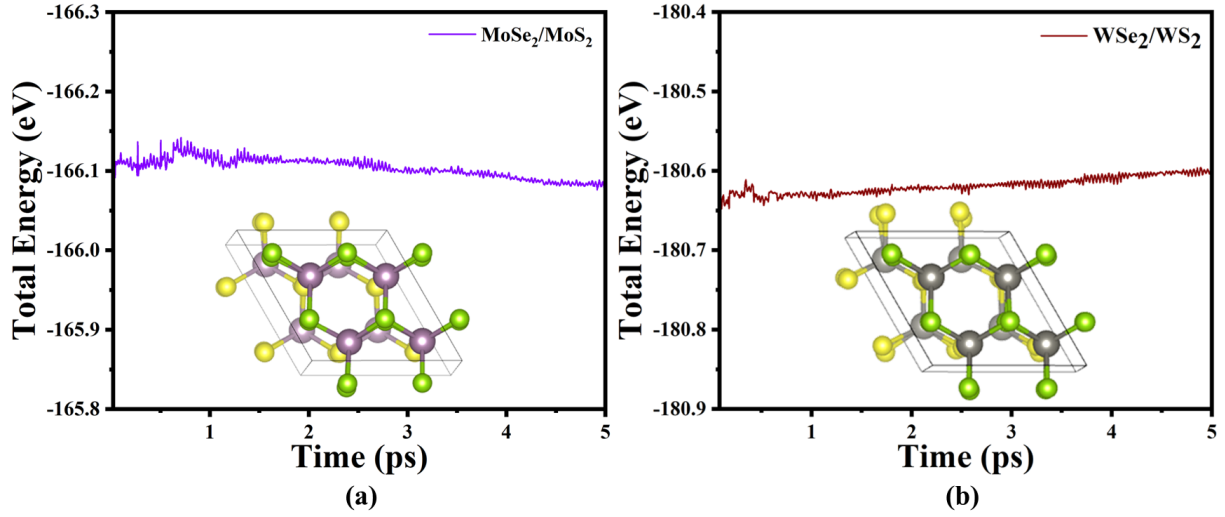


Figure 4. Total energy as a function of time steps for (a) MoSe<sub>2</sub>/MoS<sub>2</sub> and (b) WSe<sub>2</sub>/WS<sub>2</sub> systems obtained from the AIMD simulations at 500K. The resultant structures are shown in the inset. Here, purple, grey, yellow, and green spheres represent the Mo, W, S, and Se atoms, respectively.

## 2. Electronic Properties

The electronic band structures of the studied heterostructures were initially calculated using both the GGA-PBE and HSE06 functionals. To confirm the spatial separation of charge carriers, we computed the atomic orbital-projected PBE band structures, shown in Fig. S5 of the SM. These highlight the contributions of each element's valence orbitals to the energy states. The analysis reveals that the VBM and CBM belong to different layers: the VBM primarily originates from the donor layer, while the CBM is composed of the acceptor layer. This indicates that the photogenerated electrons and holes are confined to separate layers, in accordance with the type-II band alignment, confirmed previously for all six heterostructures at the HSE06 level. For example, in the MoSe<sub>2</sub>/MoS<sub>2</sub> heterostructure (see Fig. S5(b) of the SM), VBM is attributed to the MoSe<sub>2</sub> (donor) layer, while contribution to CBM comes from the MoS<sub>2</sub> (acceptor) layer. The obtained  $E_g$  values from the PBE band structures are listed in Table VI. The PBE band structures yield indirect  $E_g$  of 1.15 eV ( $\Gamma \rightarrow T$ ), 1.09 eV ( $K \rightarrow T$ ), and 0.95 eV ( $K \rightarrow T$ ), respectively for the WS<sub>2</sub>/MoS<sub>2</sub> [32, 73], MoSe<sub>2</sub>/WS<sub>2</sub> [74], and WSe<sub>2</sub>/MoSe<sub>2</sub> [32, 75] heterostructures, consistent with the literature. Some minor differences in the k-point positions for the CBM are observed, such as in the WS<sub>2</sub>/MoS<sub>2</sub>

Table VI. Calculated  $E_g$  values using the PBE and HSE06 functionals, and  $E_g^{QP}$  values using  $G_0W_0$  approximation considering 160 unoccupied bands.  $E_g^{QP}$  values are indirect in nature for all the considered heterostructures .

S.No.	Heterostructures	$E_g(\text{eV})$			$E_g^{QP}(\text{eV})$		$E_{dir}^{QP}(\text{eV})$	
		PBE	HSE06		$G_0W_0$	$G_0W_0$	$G_0W_0 + \text{SOC}$	
1	WS <sub>2</sub> /MoS <sub>2</sub>	1.15	1.75	Indirect	2.15	2.99	2.79	
2	MoSe <sub>2</sub> /MoS <sub>2</sub>	0.93	1.57	Direct	1.90	2.43	2.34	
3	MoSe <sub>2</sub> /WS <sub>2</sub>	1.09	1.60	Indirect	1.94	2.60	2.44	
4	WSe <sub>2</sub> /MoS <sub>2</sub>	0.64	1.46	Direct	2.08	2.34	2.14	
5	WSe <sub>2</sub> /MoSe <sub>2</sub>	0.95	1.43	Indirect	2.12	2.79	2.58	
6	WSe <sub>2</sub> /WS <sub>2</sub>	0.90	1.47	Direct	2.15	2.70	2.00	

heterostructure, where Amin *et al.* [32] reported a gap from  $\Gamma \rightarrow K$ , while Liang *et al.* [73] reported VBM at  $\Gamma$  and CBM at a k-point in the mid of  $\Gamma$  and K, in agreement with our results. The disagreement with the work of Amin *et al.* [32] may arise from our use of non-local vdW corrections, compared to local corrections used in their study. The direct  $E_g$  (at K) of 0.93 eV, 0.64 eV, and 0.90 eV for the MoSe<sub>2</sub>/MoS<sub>2</sub>, WSe<sub>2</sub>/MoS<sub>2</sub>, and WSe<sub>2</sub>/WS<sub>2</sub> heterostructures, respectively, are also in agreement with the previous studies [70, 76–78]. The underestimated PBE band gaps get enhanced using the HSE06 functional (see  $E_g$  values presented in Table VI). The HSE06 band structures, presented in Fig.5 show that while the conduction band shifts upward, the overall band dispersion remains unchanged, maintaining the same band gap nature as in the PBE calculations. For the WS<sub>2</sub>/MoS<sub>2</sub>, MoSe<sub>2</sub>/WS<sub>2</sub>, and WSe<sub>2</sub>/MoSe<sub>2</sub> heterostructures our HSE06 based  $E_g$  values of 1.75 eV, 1.60 eV, and 1.43 eV, respectively, are consistent with the corresponding reported gaps of 1.70 eV [32], 1.58 eV [74], 1.5 eV [32]. We further observe that, irrespective of the functional used, the highest occupied valence bands of the heterostructures are degenerate throughout the k-path  $M \rightarrow \Gamma$  and split midway through  $\Gamma \rightarrow T$ . When the same calculations are performed without including the SOC, no such splitting takes place, therefore, this splitting is clearly due to SOC. This behavior is seen for all the heterostructures under consideration.



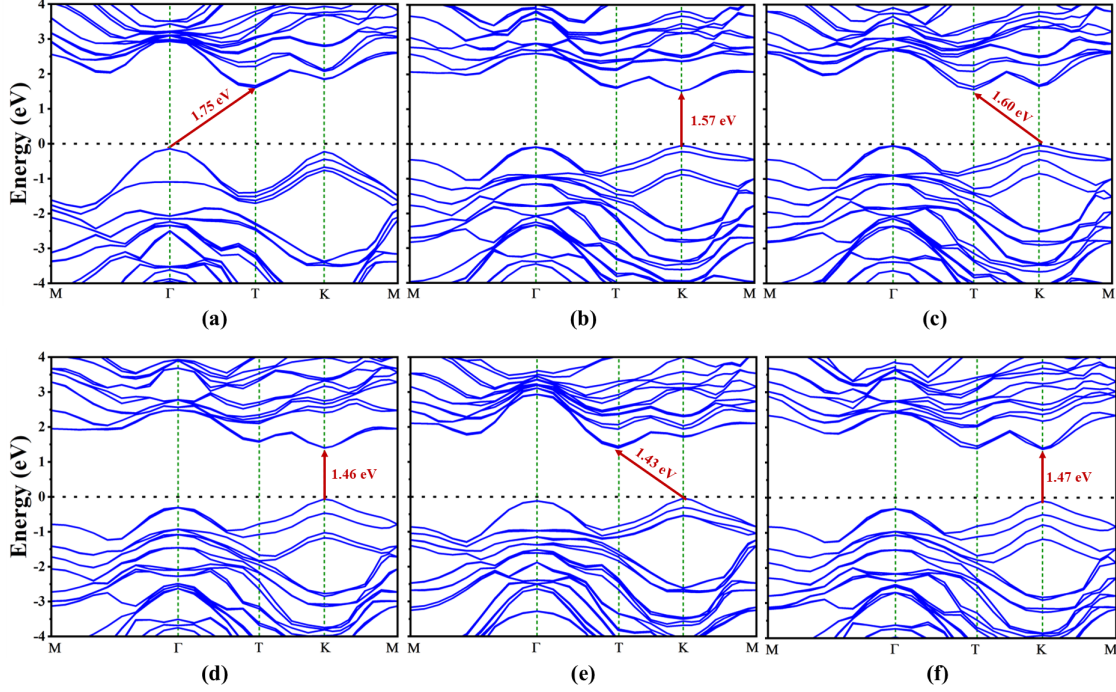


Figure 5. Calculated band structures of (a)  $\text{WS}_2/\text{MoS}_2$ , (b)  $\text{MoSe}_2/\text{MoS}_2$ , (c)  $\text{MoSe}_2/\text{WS}_2$ , (d)  $\text{WSe}_2/\text{MoS}_2$ , (e)  $\text{WSe}_2/\text{MoSe}_2$ , and (f)  $\text{WSe}_2/\text{WS}_2$  heterojunctions using the HSE06 functional.

Given the strong correlation effects observed in the QP gaps of the TMD monolayers, it is likely that these effects also play a significant role in the corresponding heterostructures. Therefore, we performed QP band structure calculations using  $G_0W_0$  approximation for all six TMD heterostructures. Initially, 160 unoccupied bands were considered, and this number was increased to 200 to check the convergence of the QP band gaps ( $E_g^{QP}$ ). The  $E_g^{QP}$  values using 160 bands are listed in Table VI, while those with 200 bands are in Table S3 of the SM. The results show almost negligible changes in  $E_g^{QP}$  with 200 bands, so we proceed with 160 unoccupied bands for further study of  $G_0W_0$  band structures for all the six heterostructures. For the purpose, a procedure identical to the case of monolayers was adopted and the corresponding Wannierized PBE band structure for  $\text{WS}_2/\text{MoS}_2$  is compared with the original band structure in Fig. S6 of the SM. The Wannier-interpolated  $G_0W_0$  band structures for all the considered heterostructures are depicted in Fig. 6. We found that for  $\text{MoSe}_2/\text{MoS}_2$ ,  $\text{WSe}_2/\text{MoS}_2$ , and  $\text{WSe}_2/\text{WS}_2$  heterostructures which showed direct gaps at the DFT level (PBE and HSE06), the CBM shifts to a lower energy at the T point in the Brillouin zone located between  $\Gamma$  and K, resulting in indirect gaps. While the other

three heterostructures, namely,  $\text{WS}_2/\text{MoS}_2$  [32, 73],  $\text{MoSe}_2/\text{WS}_2$  [74], and  $\text{WSe}_2/\text{MoSe}_2$  [32, 75], which exhibited indirect band gaps at the DFT level, retained that nature even after  $G_0W_0$  calculations. In the  $\text{WSe}_2/\text{MoS}_2$  heterostructure, after  $G_0W_0$  calculations, the VBM is shifted from K to  $\Gamma$ , compared to the HSE06 results. The  $E_g^{QP}$  values for all the heterostructures are significantly larger than those obtained from the DFT calculations, indicating strong electron correlation effects. For  $\text{WS}_2/\text{MoS}_2$  heterostructure, our calculated  $E_g^{QP}$  of 2.15 eV is in excellent agreement with the reported value of 2.10 eV [32], along with the indirect nature of the band gap. Similarly, our indirect  $E_g^{QP}$  of 2.12 eV for the  $\text{WSe}_2/\text{MoSe}_2$  heterostructure is also consistent with the literature [64]. In the  $G_0W_0$  bands of all heterostructures, a direct band gap of higher energy is present at the K high symmetry point, as is clear from Fig. 6, and the corresponding  $E_{dir}^{QP}$  values are also given in Table VI. These direct gaps are crucial for studying the optical response of the heterostructures discussed later in detail in section III D 4. The SOC effects are included in  $E_{dir}^{QP}$  (see Table VI), similar to the case of monolayers, by applying a rigid shift to the VBM and CBM, based on the shifts obtained at the GGA-PBE level.

Heterojunction formation leads to a reduction in both the DFT and  $G_0W_0$  band gaps compared to the isolated TMD monolayers. For example, the  $E_g$  ( $E_g^{QP}$ ) for isolated  $\text{WS}_2$  and  $\text{WSe}_2$  monolayers are 1.96 eV (2.76 eV) and 1.65 eV (2.17 eV), respectively. After combining these layers into the  $\text{WSe}_2/\text{WS}_2$  heterostructure, the  $E_g$  ( $E_g^{QP}$ ) decrease to 1.47 eV (2.15 eV). This reduction in band gaps due to heterojunction formation is advantageous for covering a broader solar spectrum.

The built-in electric field/voltage in a solar cell is an important quantity determining its operation by playing a key role in the separation and movement of charge carriers. Due to the horizontal mirror asymmetry of the considered heterostructures, they will have in-built electric fields in the  $z$ -direction. The electrostatic potential energy as a function of distance along the  $z$ -direction is presented in Fig.7 for the  $\text{MoSe}_2/\text{MoS}_2$  and  $\text{WSe}_2/\text{WS}_2$  heterostructures, while for the rest of the four heterostructures, it is shown in Fig. S7 of the SM. The asymmetric potential energy across the two layers gives rise to an in-built electric field ( $\mathbf{E}_{in}$ ) across each of the considered heterostructures. The difference in average potential energy across the two layers, denoted by  $\Delta E$  (see Table VII), is 3.16 eV and 3.29 eV in the case of  $\text{MoSe}_2/\text{MoS}_2$  and  $\text{WSe}_2/\text{WS}_2$  heterostructures, respectively (see Fig.7). For the other four heterostructures,  $\text{WS}_2/\text{MoS}_2$ ,  $\text{MoSe}_2/\text{WS}_2$ ,  $\text{WSe}_2/\text{MoS}_2$ , and  $\text{WSe}_2/\text{MoSe}_2$ ,

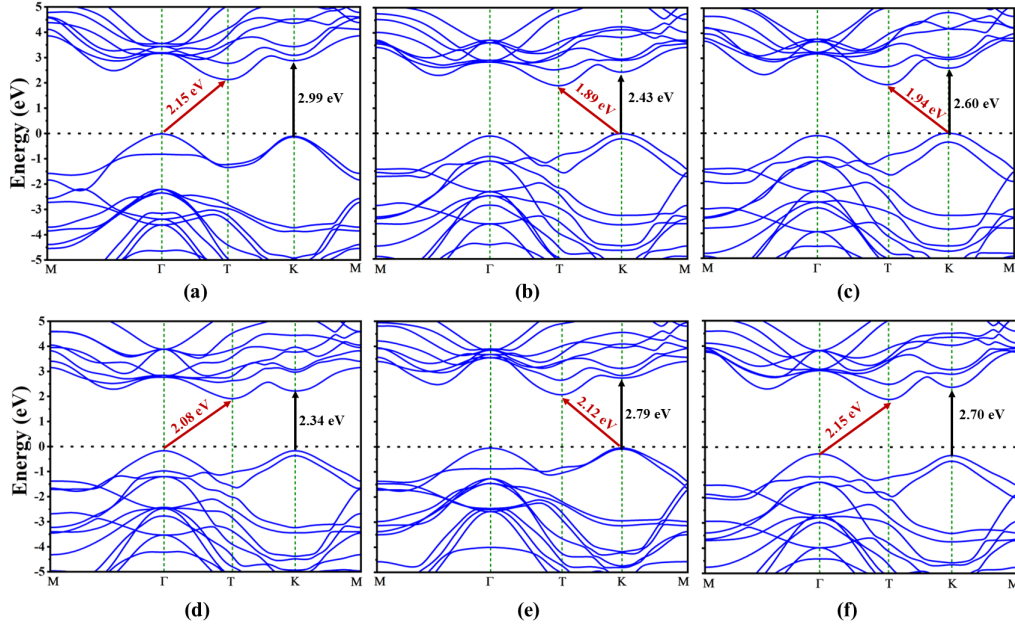


Figure 6. Calculated band structures of (a)  $\text{WS}_2/\text{MoS}_2$ , (b)  $\text{MoSe}_2/\text{MoS}_2$ , (c)  $\text{MoSe}_2/\text{WS}_2$ , (d)  $\text{WSe}_2/\text{MoS}_2$ , (e)  $\text{WSe}_2/\text{MoSe}_2$ , and (f)  $\text{WSe}_2/\text{WS}_2$  heterojunctions using  $G_0W_0$  approximation.

$\Delta E$  of 0.08 eV, 3.31 eV, 3.17 eV, and 0.06 eV are obtained, respectively. The quite small  $\Delta E$  values in the case of  $\text{WS}_2/\text{MoS}_2$  and  $\text{WSe}_2/\text{MoSe}_2$  heterostructures are due to the presence of similar chalcogen atoms in both the constituent monolayers, whereas, comparatively large  $\Delta E$  values in case of other heterostructures arises due to the electronegativity differences ( $\text{S} > \text{Se}$ ). Using the  $\Delta E$  values,  $\mathbf{E}_{in}$  is calculated, and their values (see Table VII), as expected, are significant only for those four heterostructures ( $\text{MoSe}_2/\text{MoS}_2$ ,  $\text{MoSe}_2/\text{WS}_2$ ,  $\text{WSe}_2/\text{MoS}_2$ , and  $\text{WSe}_2/\text{WS}_2$ ) for which  $\Delta E$  is large. This intrinsic electric field helps to spatially separate the photogenerated charge carriers because, under its influence, the electrons and holes move in opposite directions. This separation of charges is crucial for the generation of an electric current when an external circuit is connected to the solar cell. In a sense, the built-in electric field provides the initial push for the flow of electrons, thus enabling the conversion of light energy into electrical energy. Clearly, higher built-in electric fields will lead to highly efficient solar cell devices.

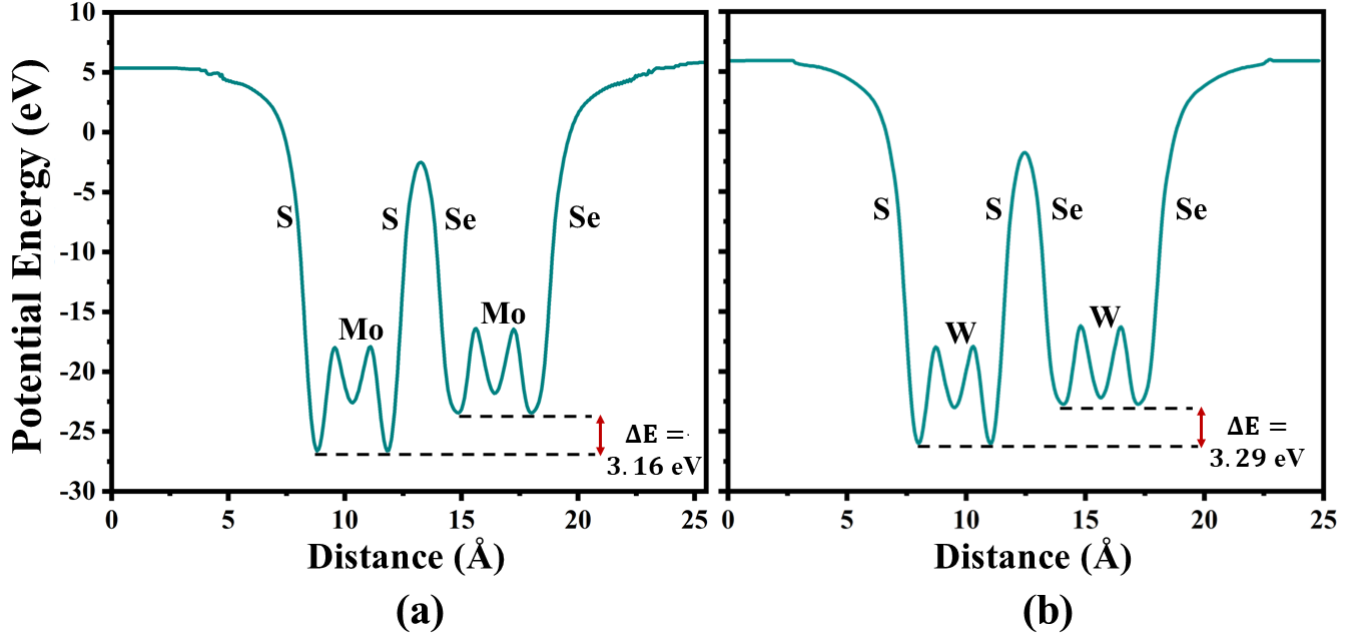


Figure 7. Electrostatic potential energy as a function of distance along  $z$ -direction for (a)  $\text{MoSe}_2/\text{MoS}_2$  and (b)  $\text{WSe}_2/\text{WS}_2$  heterojunctions.  $\Delta E$  denotes the difference in average electrostatic potential energy across the layers.

### 3. Effective masses of charge carriers

The effective masses of the charge carriers of a semiconductor determine their mobility, and, thus the performance of a solar cell composed of it. In this work, we have computed the effective masses of both the electrons ( $m_e^*$ ) and holes ( $m_h^*$ ) by employing the parabolic approximation around the CBM and VBM, respectively. The following equation is used for calculating the elements of the effective mass tensor:

$$m_{ij}^*(\mathbf{k}) = \hbar^2 \left( \frac{\partial^2 (E(\mathbf{k}))}{\partial k_i \partial k_j} \right)_{\mathbf{k}=\mathbf{K}_0}^{-1} m_0 \quad (5)$$

where  $\hbar$  is the reduced Planck's constant,  $\mathbf{k}$  is a vector in the first Brillouin zone, and  $E(\mathbf{k})$  is the corresponding valence/conduction band Kohn-Sham eigenvalue.  $\mathbf{K}_0$  represents the band extremum location in the band structure of all the considered heterostructures,  $i, j$  are Cartesian directions, and  $m_0$  denotes the free electron mass. Because of the isotropic nature of these materials, there is only one unique nonzero “in plane” element of the effective-mass tensor of the holes and electrons of each heterostructure, which we report in Table VII. The

effective masses are calculated at the CBM and VBM along specific  $k$  directions specified in the parenthesis next to them. For instance, in the WSe<sub>2</sub>/MoSe<sub>2</sub> heterostructure,  $m_e^*$  ( $m_h^*$ ) is calculated along the high symmetry directions T $\rightarrow$   $\Gamma$  (K $\rightarrow$ T) and T $\rightarrow$ K (K $\rightarrow$ M). Furthermore, we have compared these effective masses with those of involved monolayers, provided in Table S2 of the SM [79]. We note that the calculated values of the effective masses in most of the considered heterostructures are close to their values in the constituent monolayers, except for WS<sub>2</sub>/MoS<sub>2</sub>, for which  $m_h^*$  for the heterostructure is comparatively larger. Smaller  $m_e^*$  and  $m_h^*$  values indicate higher carrier mobilities, which improve both carrier current and photogenerated charge separation. Ideally,  $m_e^*$  and  $m_h^*$  should be of similar magnitudes to ensure balanced carrier mobilities in opposite directions, reducing electron-hole recombination rate. We found that in WSe<sub>2</sub>/MoS<sub>2</sub>, WSe<sub>2</sub>/MoSe<sub>2</sub>, and WSe<sub>2</sub>/WS<sub>2</sub> heterostructures,  $m_e^*$  and  $m_h^*$  are smaller compared to those for the other heterostructures and nearly equal, suggesting better solar cell performance.

Table VII. The difference in average electrostatic potential energy across the layers ( $\Delta E$ ), in-built electric field ( $\mathbf{E}_{in}$ ), and the computed effective masses of electrons ( $m_e^*$ ) and holes ( $m_h^*$ ) in the units of the free-electron mass,  $m_0$  for the heterojunctions under consideration.

S.No.	Heterojunction	$\Delta E$ (eV)	$\mathbf{E}_{in}$ (V/Å)	$m_e^*(m_0)$		$m_h^*(m_0)$	
1	WS <sub>2</sub> /MoS <sub>2</sub>	0.08	0.01	0.53(T $\rightarrow$ $\Gamma$ )	0.60(T $\rightarrow$ K)	0.86( $\Gamma \rightarrow$ M)	0.86( $\Gamma \rightarrow$ T)
2	MoSe <sub>2</sub> /MoS <sub>2</sub>	3.16	0.34	0.45(K $\rightarrow$ T)	0.49(K $\rightarrow$ M)	0.70(K $\rightarrow$ T)	0.89(K $\rightarrow$ M)
3	MoSe <sub>2</sub> /WS <sub>2</sub>	3.31	0.36	0.48(T $\rightarrow$ $\Gamma$ )	0.53(T $\rightarrow$ K)	0.69(K $\rightarrow$ T)	0.78(K $\rightarrow$ M)
4	WSe <sub>2</sub> /MoS <sub>2</sub>	3.17	0.34	0.43(K $\rightarrow$ T)	0.46(K $\rightarrow$ M)	0.43(K $\rightarrow$ T)	0.48(K $\rightarrow$ M)
5	WSe <sub>2</sub> /MoSe <sub>2</sub>	0.06	0.01	0.47(T $\rightarrow$ $\Gamma$ )	0.49(T $\rightarrow$ K)	0.39(K $\rightarrow$ T)	0.44(K $\rightarrow$ M)
6	WSe <sub>2</sub> /WS <sub>2</sub>	3.29	0.36	0.36(K $\rightarrow$ T)	0.39(K $\rightarrow$ M)	0.43(K $\rightarrow$ T)	0.48(K $\rightarrow$ M)

#### 4. Optical Properties

After exploring the electronic properties, our study focuses on the optical response of the heterostructures under consideration. For the study of optical properties, we have employed BSE as given by Eq.2. Similar to monolayers,  $\epsilon_{Im}(\omega)$  is plotted against the incident photon energy for each heterostructure, as depicted in Fig. 8. It is to be noted that the nature

of  $E_g^{QP}$  computed using the  $G_0W_0$  approximation (on the top of which the BSE calculations are performed) is indirect for all the six heterostructures. As a result, the optical transitions corresponding to these gaps are not reflected in the optical absorption spectra, and the transitions corresponding to  $E_{dir}^{QP}$  (at K, shown by an arrow in Fig. 6) dominate the computed BSE spectra presented in Fig. 8. The first optically active peak arises by excitonic transitions, and corresponds to the optical gaps ( $E_g^{op}$ ) listed in Table VIII. These  $E_g^{op}$  values lie in the visible spectrum, with the coverage of about half of the visible range (highlighted in the figure), which is the focus of this work because of its possible solar-cell applications. For the  $\text{MoSe}_2/\text{MoS}_2$  heterostructure,  $E_g^{op}$  of 2.04 eV is close to the reported photoluminescence (PL) peak of 1.89 eV [33], validating our calculations. Further, we added the effect of SOC in all the  $E_g^{op}$  values as done in the  $E_g^{QP}$  values of the studied heterostructures. The resultant  $E_g^{op}$  values at the BSE+SOC level are also listed in the same table. Remarkably, the SOC-corrected BSE gives  $E_g^{op}$  of 1.95 eV for the  $\text{MoSe}_2/\text{MoS}_2$  heterostructure aligns even better with the reported PL peak [33]. The  $E_{ex}$  is also calculated for each of the heterostructure, and the obtained values are in the range of 0.22 eV – 0.62 eV. We observe that in most of the cases,  $E_{ex}$  is smaller in heterostructures as compared to the constituent monolayers, such as 0.39 eV for the  $\text{MoSe}_2/\text{MoS}_2$  heterostructure versus 0.46 eV for the  $\text{MoSe}_2$  and  $\text{MoS}_2$  monolayers. The lower  $E_{ex}$  results from increased screening due to heterostructure formation, leading to weaker exciton binding, and thus easier separation of the photogenerated charge carriers.

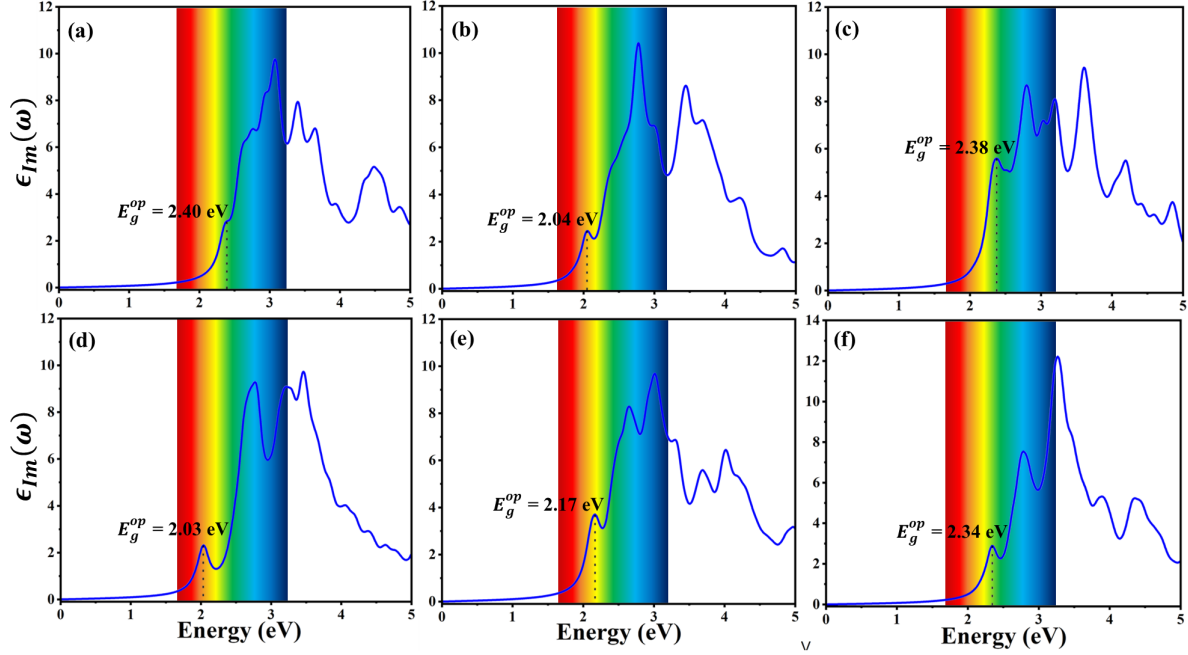


Figure 8. Imaginary part of the dielectric function,  $\epsilon_{Im}(\omega)$  as a function of the energy of the incident photon for (a) WS<sub>2</sub>/MoS<sub>2</sub>, (b) MoSe<sub>2</sub>/MoS<sub>2</sub>, (c) MoSe<sub>2</sub>/WS<sub>2</sub>, (d) WSe<sub>2</sub>/MoS<sub>2</sub>, (e) WSe<sub>2</sub>/MoSe<sub>2</sub>, and (f) WSe<sub>2</sub>/WS<sub>2</sub> heterostructures calculated using BSE.

Table VIII. Calculated optical gaps,  $E_g^{op}$  from the BSE calculations and the corresponding exciton binding energies,  $E_{ex}$  for the TMD heterostructures under consideration.

S.No.	Heterostructures	$E_g^{op}$ (eV)		$E_{ex}$ (eV)
		BSE	BSE+SOC	
1	WS <sub>2</sub> /MoS <sub>2</sub>	2.40	2.20	0.59
2	MoSe <sub>2</sub> /MoS <sub>2</sub>	2.04	1.95	0.39
3	MoSe <sub>2</sub> /WS <sub>2</sub>	2.38	2.22	0.22
4	WSe <sub>2</sub> /MoS <sub>2</sub>	2.03	1.83	0.31
5	WSe <sub>2</sub> /MoSe <sub>2</sub>	2.17	1.96	0.62
6	WSe <sub>2</sub> /WS <sub>2</sub>	2.34	1.64	0.36

### 5. Power Conversion Efficiencies (PCE)

The power-conversion efficiency (PCE) of a solar device, as its name suggests, is a measure of how efficiently it converts the solar energy into the electrical energy. To calculate PCE, a method proposed by Scharber *et al.* [80] has been widely used, according to which the maximum PCE under the 100% external quantum efficiency (EQE) can be determined as

$$PCE = \frac{V_{oc}J_{sc}\beta_{FF}}{P_{solar}} = \frac{0.65(E_g^d - \Delta E_c - 0.3) \int_{E_g^d}^{\infty} \frac{P(\hbar\omega)}{\hbar\omega} d\omega}{\int_0^{\infty} P(\hbar\omega) d\omega}, \quad (6)$$

where 0.65 is the band-fill factor denoted by  $\beta_{FF}$ ,  $V_{oc} = (E_g^d - \Delta E_c - 0.3)$  is an estimate of the open circuit voltage, with  $E_g^d$  and  $\Delta E_c$  representing the band gap of donor and the conduction band offset between the donor and acceptor semiconductors, respectively,  $P(\hbar\omega)$ , expressed in the units  $\text{Wm}^{-2}\text{eV}^{-1}$ , is the AM1.5 solar energy flux for energy  $\hbar\omega$  of the photon. Further,  $J_{sc}$  is the short circuit current density evaluated as the integral  $J_{sc} = \int_{E_g^d}^{\infty} \frac{P(\hbar\omega)}{\hbar\omega} d\omega$ ,

, under the assumption of 100% EQE. The integral in the denominator  $\int_0^{\infty} P(\hbar\omega) d\omega$  is the total power of the incident solar radiation. To date, reported PCEs for various materials in numerous studies were calculated at the DFT level only, using the hybrid functionals [29, 81, 82]. Following this, we calculated PCEs using the HSE06 functional and compared our results with those in the literature for different heterojunction solar cells. Additionally, we also computed PCE for the TMD heterostructures at the  $G_0W_0$  level for completeness. To summarize, we compute PCE in the following three ways: (a) at the DFT level using the HSE06 functional, (b) at the  $G_0W_0$  level without SOC, and (c) at the  $G_0W_0$  level with SOC. For the latter two methods, we used  $E_g^{op}$  from BSE as  $E_g^d$ , instead of  $E_g^{QP}$ , because  $E_g^{op}$  calculated from BSE more accurately reflects experimental values due to its inclusion of electron-hole attraction effects. Further, the BSE optical gap is independent of the vacuum used in calculations, unlike the GW QP gap [70]. The resulting PCEs calculated using Eq. 6 are summarized in Table IX, with the required intermediate parameters ( $E_g^d$ ,  $\Delta E_c$ ,  $V_{oc}$ , and  $J_{sc}$ ) provided in Tables S4, S5, and S6 of the SM. PCE is not calculated at the  $G_0W_0$  level for  $\text{MoSe}_2/\text{WS}_2$  because of its failure to show type II band alignment, as discussed earlier. We obtained PCEs in the ranges of 12.93% – 19.25%, 6.54% – 14.79% , and 7.48% – 15.25%



for the considered heterostructures using HSE06,  $G_0W_0$ , and  $G_0W_0 + \text{SOC}$ , respectively. For each heterostructure, the PCE order is  $\text{HSE06} > G_0W_0 + \text{SOC} > G_0W_0$ , which is reverse of the band gap order. This is because increasing the donor band gap narrows the range of the solar spectrum coverage during absorption, because in that case only photons of energies higher than the gap will be useful. From Eq. 6, it is obvious that in order to have high values of PCE, both  $\Delta E_c$  and  $E_g^d$  should be small, because lower  $\Delta E_c$  leads to higher  $V_{oc}$ , while a lower  $E_g^d$  gives rise to a higher  $J_{sc}$ . It is to be noted that at the HSE06 level, a minimum value of both  $\Delta E_c$  (0.11 eV) and  $E_g^d$  (1.65 eV) for the  $\text{WSe}_2/\text{WS}_2$  heterostructure, resulted in maximum PCE of 19.25%. At the  $G_0W_0$  and  $G_0W_0 + \text{SOC}$  levels, both  $\Delta E_c$  and  $E_g^d$  are minimum for the  $\text{MoSe}_2/\text{MoS}_2$  heterostructure, giving maximum PCEs of 14.79%, and 15.25%, respectively. If we compare the cases of  $\text{WSe}_2/\text{MoS}_2$ ,  $\text{WSe}_2/\text{MoSe}_2$ , and  $\text{WSe}_2/\text{WS}_2$  structures, where the donor semiconductor is the same ( $\text{WSe}_2$ ), the highest PCE from all the three methods corresponds to the lowest  $\Delta E_c$  and vice-versa. It is worth mentioning that our calculated PCEs are significantly higher than those reported in experimental studies [83]. For instance, experimental PCEs for the  $\text{WSe}_2/\text{MoS}_2$  (0.2%) and  $\text{WSe}_2/\text{MoSe}_2$  (0.12%) heterostructures are much lower because they were measured under EQE of 1.5% and 1.2%, respectively [84, 85]. However, it is not possible to calculate EQE theoretically, therefore the PCEs are computed using Eq. 6 which assumes 100% EQE. These theoretical PCEs computed assuming ideal conditions provide insights into the comparative performance of materials for solar energy harvesting, guiding experimentalists in selecting materials for solar cell design. Among the studied heterostructures,  $\text{MoSe}_2/\text{MoS}_2$  and  $\text{WSe}_2/\text{WS}_2$  are most preferable candidates for heterojunction solar cells due to their maximum PCE of 18.64% and 19.25% (at the HSE06 level), respectively. In table X we list the PCEs of some recently proposed heterojunction solar cell devices, calculated at the DFT level using hybrid functional, and find that the highest PCE (19.25%) among our heterostructures is: (a) larger than most of the values reported in the table, and (b) very close to the highest reported values.

Table IX. Calculated power conversion efficiencies (PCE) of the heterostructures under consideration.

S.No.	Heterostructures	PCE (%)		
		HSE06	$G_0W_0$	$G_0W_0 + \text{SOC}$
1	$\text{WS}_2/\text{MoS}_2$	12.93	9.40	12.27
2	$\text{MoSe}_2/\text{MoS}_2$	18.64	14.79	15.25
3	$\text{MoSe}_2/\text{WS}_2$	17.79		
4	$\text{WSe}_2/\text{MoS}_2$	14.35	6.54	7.48
5	$\text{WSe}_2/\text{MoSe}_2$	16.15	9.30	11.82
6	$\text{WSe}_2/\text{WS}_2$	19.25	9.65	12.00

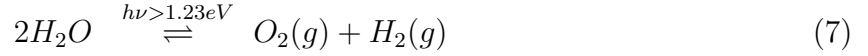
Table X. Power conversion efficiencies (PCE) of some heterojunction solar cells proposed in the literature.

Heterojunction solar cells	PCE (%)	References
Phosphorene/MoS <sub>2</sub> heterobilayer	11.5-17.5	[81]
MoS <sub>2</sub> /bilayer phosphorene	16-18	[27]
CBN/PCBM heterojunctions	10-20	[86]
$\alpha$ -As/ $\alpha$ -AsP bilayer	21.3	[87]
Graphene/GaAs	18.5	[88]
MoS <sub>2</sub> / $\psi$ -phosphorene	20.26	[28]
TiNF/TiNBr	18	[82]
TiNCl/TiNBr	19	[82]
TiNF/TiNCl	22	[82]
Te/MoS <sub>2</sub>	10.6	[29]
Te/MoSe <sub>2</sub>	17.5	[29]
Te/WS <sub>2</sub>	18.8	[29]
Te/WSe <sub>2</sub>	18.7	[29]
Te/MoTe <sub>2</sub>	20.1	[29]
Te/WTe <sub>2</sub>	22.5	[29]
WS <sub>2</sub> /MoS <sub>2</sub>	12.93	This study
MoSe <sub>2</sub> /MoS <sub>2</sub>	18.64	This study
MoSe <sub>2</sub> /WS <sub>2</sub>	17.79	This study
WSe <sub>2</sub> /MoS <sub>2</sub>	14.35	This study
WSe <sub>2</sub> /MoSe <sub>2</sub>	16.15	This study
WSe <sub>2</sub> /WS <sub>2</sub>	19.25	This study

### 6. Prediction of photocatalytic activity

After thoroughly investigating the photovoltaics related properties of the considered TMD heterostructures, here we briefly discuss their photocatalytic properties for hydrogen generation. Photocatalysis which relies on the photogenerated electrons and holes, is an efficient

approach for hydrogen evolution through water splitting. This process involves oxidation and reduction half-cell reactions, with the overall redox reaction represented as:



Experimental data have shown that the equilibrium potentials for the reduction ( $H^+/H_2$ ) and oxidation ( $O_2/H_2O$ ) reactions under standard conditions are -4.44 V and -5.67 V, respectively [89]. Consequently, the potential difference for the corresponding redox reaction, i.e.,  $V_{H^+/H_2} - V_{O_2/H_2O}$  equals 1.23 V. This indicates that for a material to serve as an effective photocatalyst, it must possess a minimum band gap of 1.23 eV. Notably, all the six TMD heterostructures investigated, meet this band gap criterion according to both the HSE06 and  $G_0W_0$  results. Therefore, all six TMD heterostructures, qualify as photocatalysts for water-splitting according to the band gap criteria. Additionally, according to the Goldilocks principle, an efficient photocatalyst should possess low recombination rate for which type II band alignment is preferable [90]. Therefore,  $MoSe_2/WS_2$  will not be efficient as a photocatalyst because of its predicted type I band alignment obtained from  $G_0W_0$  approximation. Furthermore, it is essential to note that while the minimum band gap criterion is necessary, it is not a sufficient condition for a material to be an efficient photocatalyst. Another crucial factor is the band alignment, referring to the alignment of CBM and VBM edges with the reduction and oxidation potentials of the overall redox reaction (Eq. 7). According to the band alignment condition, CBM (VBM) energy level should be less (more) negative than the reduction (oxidation) energy level. This necessitates that both the potential levels of the redox reaction should lie within the CBM and VBM levels, in addition to having a gap larger than 1.23 eV. Therefore, to check the band alignment for photocatalysis, we have calculated band edges,  $E_{CBM}$  and  $E_{VBM}$ , at the HSE06 and  $G_0W_0$  level, provided in Table XI and also depicted in Fig. 9. First discussing the HSE06 results, we observe that none of the considered heterostructures, satisfy the band alignment criteria. Except  $MoSe_2/MoS_2$ ,  $E_{CBM}$  in other five heterostructures meets the band gap criterion as it is less negative than the reduction potential and thus possesses strong reducing ability, however,  $E_{VBM}$  fails to meet the condition. In the  $MoSe_2/MoS_2$  heterostructure,  $E_{VBM}$  aligns with the oxidation level according to the given criterion and possesses good oxidizing ability, but,  $E_{CBM}$  is more negative than the reduction potential. Next, considering the band edge positions obtained at the  $G_0W_0$  level, we find that three heterostructures, namely,  $WS_2/MoS_2$ ,  $MoSe_2/MoS_2$ ,

and  $\text{WSe}_2/\text{MoS}_2$ , meet the band alignment criteria and possess both the reducing and oxidizing capabilities. The rest three heterostructures, partially satisfy the criteria, i.e., from the CBM side only. Therefore, from our  $G_0W_0$  calculations, we find that the  $\text{WS}_2/\text{MoS}_2$ ,  $\text{MoSe}_2/\text{MoS}_2$ , and  $\text{WSe}_2/\text{MoS}_2$  heterostructures possess the following three properties: (a) band gap  $> 1.23$  eV, (b) type II band alignment, and (c) meet the band alignment criteria. Following this, we infer that these three heterostructures are promising candidates for efficient photocatalysis.

Table XI. Calculated values of band edges,  $E_{CBM}$  and  $E_{VBM}$ , of the considered TMD heterojunctions at the HSE06 and  $G_0W_0$  level. The values are calculated with respect to vacuum level.

S.No.	Heterostructures	$E_{VBM}$ (eV)		$E_{CBM}$ (eV)	
		HSE06	$G_0W_0$	HSE06	$G_0W_0$
1	$\text{WS}_2/\text{MoS}_2$	-5.643	-5.813	-3.890	-3.662
2	$\text{MoSe}_2/\text{MoS}_2$	-6.615	-5.727	-5.040	-3.834
3	$\text{WSe}_2/\text{MoS}_2$	-5.475	-5.775	-4.001	-3.698
4	$\text{WSe}_2/\text{MoSe}_2$	-5.154	-5.384	-3.718	-3.444
5	$\text{WSe}_2/\text{WS}_2$	-5.445	-5.614	-3.972	-3.459
6	$\text{MoSe}_2/\text{WS}_2$	-5.424	-5.556	-3.825	-3.619

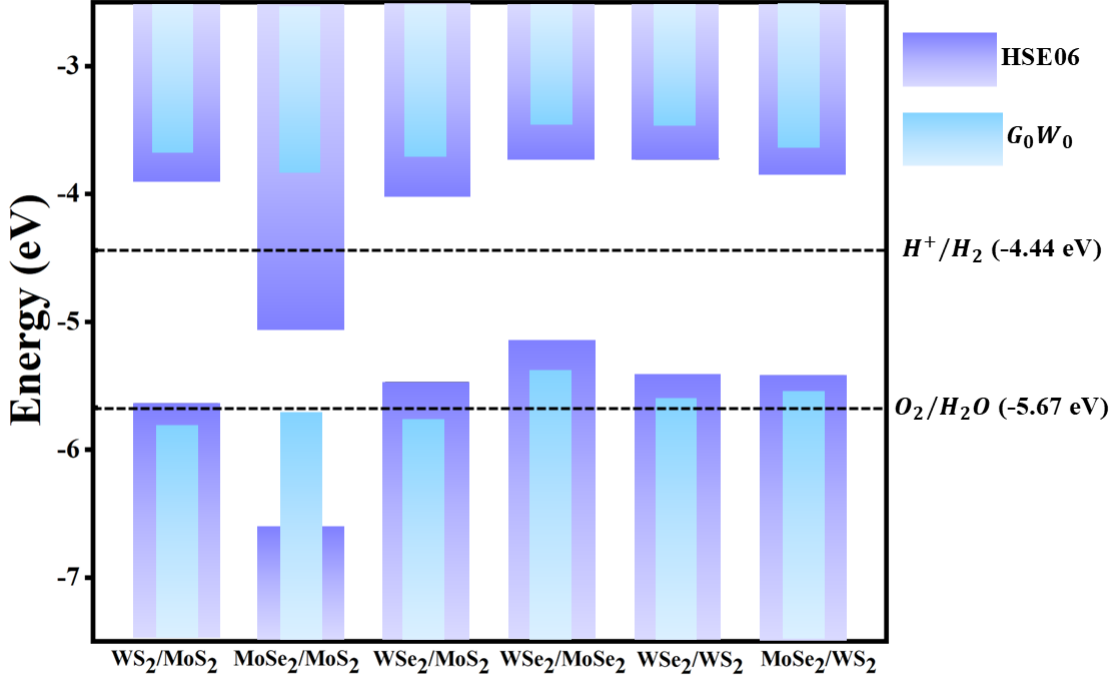


Figure 9. Band edge positions of the considered TMD heterostructures with respect to vacuum at the HSE06 and  $G_0W_0$  level. The redox potential levels are also shown by dashed lines.

#### IV. CONCLUSION

To summarize, we have proposed 2D transition-metal dichalcogenides based vertical bilayer heterostructures for solar cell devices using first-principles DFT and many body perturbation based  $G_0W_0$ -BSE calculations. Using four TMD monolayers (MoS<sub>2</sub>, WS<sub>2</sub>, MoSe<sub>2</sub>, and WSe<sub>2</sub>) which satisfy the lattice mismatch condition, six such heterostructures can be created. Among the six possible heterostructures, five namely, WS<sub>2</sub>/MoS<sub>2</sub>, MoSe<sub>2</sub>/MoS<sub>2</sub>, WSe<sub>2</sub>/MoS<sub>2</sub>, WSe<sub>2</sub>/MoSe<sub>2</sub>, and WSe<sub>2</sub>/WS<sub>2</sub>, meet the criterion of type II band alignment according to both the HSE06 functional and  $G_0W_0$  approximation, whereas, MoSe<sub>2</sub>/WS<sub>2</sub> shows type II band alignment at the HSE06 level only. We have examined the structural stability of the considered heterostructures, after which a detailed systematic investigation of their electronic structures is performed using both the DFT and  $G_0W_0$  approximation. As compared to the isolated monolayers, the considered heterostructures exhibit reduced electronic gaps, leading to wider coverage of solar spectrum. The spatial separation of photogenerated charge carriers, which is confirmed by the orbital projected PBE band structures, will lower

the electron-hole recombination rate. The calculated values of the electron and hole effective masses are small and nearly equal, which will facilitate their flow with same mobility in the opposite directions, further lowering the recombination rates. The built-in electric fields, which arises due to the horizontal mirror asymmetry in the considered heterostructures, are also computed, and found to be quite significant. It is noteworthy that these intrinsic electric fields will also lead to charge separation, and, thus, lower recombination rates. The optical responses are obtained by solving the BSE, and the PCEs are also computed at both the HSE06 and  $G_0W_0$  level. The PCE is not evaluated for  $\text{MoSe}_2/\text{WS}_2$  at the  $G_0W_0$  level because it does not manifest type II band alignment. Our study demonstrates that by carefully designing Type II heterostructures using TMD monolayers, it is possible to tailor their properties so that they will exhibit low recombination losses and high PCEs (near 20% at the HSE06 level) leading to superior solar cells.

Afterwards, the six TMD heterostructures under consideration are evaluated for their potential to function as photocatalysts for hydrogen evolution via water splitting, and  $\text{WS}_2/\text{MoS}_2$ ,  $\text{MoSe}_2/\text{MoS}_2$ , and  $\text{WSe}_2/\text{MoS}_2$  heterostructures are found to be quite promising.

In this paper we have made a number of predictions regarding the photovoltaic and photocatalytic abilities of the six TMD heterostructures, and we hope they will be tested in future experiments.

Moreover, in this work, we considered no relative rotation between the monolayers constituting the heterostructures. However, given the current interest in Moire physics induced by a relative twist angle between the layers, in future we intend to undertake a systematic study of its influence on various properties of such TMD heterojunctions.

## ACKNOWLEDGMENTS

One of the authors, K.D. acknowledges financial assistance from the Prime Minister Research Fellowship (PMRF ID-1302054), MHRD, India, and Space Time computational facility of Indian Institute of Technology Bombay. R.Y. acknowledges the support through the Insti-

tute Post-Doctoral Fellowship (IPDF) of Indian Institute of Technology Bombay.

---

- [1] Jinlong Gong, Can Li, and Michael R. Wasielewski. Advances in solar energy conversion. *Chem. Soc. Rev.*, 48:1862–1864, 2019.
- [2] Syed Ossama Ali Ahmad, Atif Ashfaq, Muhammad Usama Akbar, Mujtaba Ikram, Karim Khan, Feng Wang, Muhammad Ikram, and Asif Mahmood. Application of two-dimensional materials in perovskite solar cells: recent progress, challenges, and prospective solutions. *J. Mater. Chem. C*, 9:14065–14092, 2021.
- [3] Muhammad Zahir Iqbal and Assad-Ur Rehman. Recent progress in graphene incorporated solar cell devices. *Solar Energy*, 169:634–647, 2018.
- [4] Deep Jariwala, Vinod K. Sangwan, Lincoln J. Lauhon, Tobin J. Marks, and Mark C. Hersam. Emerging device applications for semiconducting two-dimensional transition metal dichalcogenides. *ACS Nano*, 8(2):1102–1120, Feb 2014.
- [5] Vellayappan Dheivanayagam S Ganesan, Jiajun Linghu, Chun Zhang, Yuan Ping Feng, Lei Shen, et al. Heterostructures of phosphorene and transition metal dichalcogenides for excitonic solar cells: A first-principles study. *Applied Physics Letters*, 108(12), 2016.
- [6] Yalan Zhang and Nam-Gyu Park. Quasi-two-dimensional perovskite solar cells with efficiency exceeding 22%. *ACS Energy Letters*, 7(2):757–765, Feb 2022.
- [7] Zhong-Shuai Wu, Wencai Ren, Libo Gao, Jinping Zhao, Zongping Chen, Bilu Liu, Daiming Tang, Bing Yu, Chuanbin Jiang, and Hui-Ming Cheng. Synthesis of graphene sheets with high electrical conductivity and good thermal stability by hydrogen arc discharge exfoliation. *ACS Nano*, 3(2):411–417, Feb 2009.
- [8] Sajedeh Manzeli, Dmitry Ovchinnikov, Diego Pasquier, Oleg V. Yazyev, and Andras Kis. 2d transition metal dichalcogenides. *Nature Reviews Materials*, 2(8):17033, Jun 2017.
- [9] K. S. Novoselov, A. Mishchenko, A. Carvalho, and A. H. Castro Neto. 2d materials and van der waals heterostructures. *Science*, 353(6298):aac9439, 2016.
- [10] A. K. Geim and I. V. Grigorieva. Van der waals heterostructures. *Nature*, 499(7459):419–425, Jul 2013.



- [11] Fang Wu, Yunfei Liu, Guanxia Yu, Dingfeng Shen, Yunlu Wang, and Erjun Kan. Visible-light-absorption in graphitic c3n4 bilayer: Enhanced by interlayer coupling. *The Journal of Physical Chemistry Letters*, 3(22):3330–3334, Nov 2012.
- [12] Aijun Du, Stefano Sanvito, Zhen Li, Dawei Wang, Yan Jiao, Ting Liao, Qiao Sun, Yun Hau Ng, Zhonghua Zhu, Rose Amal, and Sean C. Smith. Hybrid graphene and graphitic carbon nitride nanocomposite: Gap opening, electron–hole puddle, interfacial charge transfer, and enhanced visible light response. *Journal of the American Chemical Society*, 134(9):4393–4397, Mar 2012.
- [13] Junfeng Zhang, Weiyu Xie, Jijun Zhao, and Shengbai Zhang. Band alignment of two-dimensional lateral heterostructures. *2D Materials*, 4(1):015038, dec 2016.
- [14] Wonbong Choi, Nitin Choudhary, Gang Hee Han, Juhong Park, Deji Akinwande, and Young Hee Lee. Recent development of two-dimensional transition metal dichalcogenides and their applications. *Materials Today*, 20(3):116–130, 2017.
- [15] Sohail Ahmed and Jiabao Yi. Two-dimensional transition metal dichalcogenides and their charge carrier mobilities in field-effect transistors. *Nano-Micro Letters*, 9(4):50, Aug 2017.
- [16] Xian Wu, Haojie Zhao, Enze Zhou, Yixuan Zou, Shanpeng Xiao, Shuai Ma, Rui You, and Peng Li. Two-dimensional transition metal dichalcogenide tunnel field-effect transistors for biosensing applications. *ACS Applied Materials & Interfaces*, 15(19):23583–23592, May 2023.
- [17] Fangsheng Qian, Xiaobo Bu, Junjie Wang, Jing-Yu Mao, Su-Ting Han, and Ye Zhou. Transistors and logic circuits enabled by 2d transition metal dichalcogenides: a state-of-the-art survey. *J. Mater. Chem. C*, 10:17002–17026, 2022.
- [18] Qing Hua Wang, Kourosh Kalantar-Zadeh, Andras Kis, Jonathan N. Coleman, and Michael S. Strano. Electronics and optoelectronics of two-dimensional transition metal dichalcogenides. *Nature Nanotechnology*, 7(11):699–712, Nov 2012.
- [19] Faiha Mujeeb, Poulab Chakrabarti, Vikram Mahamiya, Alok Shukla, and Subhabrata Dhar. Influence of defects on the valley polarization properties of monolayer mos<sub>2</sub> grown by chemical vapor deposition. *Phys. Rev. B*, 107:115429, Mar 2023.
- [20] Kathleen M. McCreary, Aubrey T. Hanbicki, Glenn G. Jernigan, James C. Culbertson, and Berend T. Jonker. Synthesis of large-area ws<sub>2</sub> monolayers with exceptional photoluminescence. *Scientific Reports*, 6(1):19159, Jan 2016.

- [21] Xingli Wang, Yongji Gong, Gang Shi, Wai Leong Chow, Kuntal Keyshar, Gonglan Ye, Robert Vajtai, Jun Lou, Zheng Liu, Emilie Ringe, Beng Kang Tay, and Pulickel M. Ajayan. Chemical vapor deposition growth of crystalline monolayer  $\text{MoS}_2$ . *ACS Nano*, 8(5):5125–5131, May 2014.
- [22] Jing-Kai Huang, Jiang Pu, Chang-Lung Hsu, Ming-Hui Chiu, Zhen-Yu Juang, Yung-Huang Chang, Wen-Hao Chang, Yoshihiro Iwasa, Taishi Takenobu, and Lain-Jong Li. Large-area synthesis of highly crystalline  $\text{WSe}_2$  monolayers and device applications. *ACS Nano*, 8(1):923–930, Jan 2014.
- [23] Kin Fai Mak, Changgu Lee, James Hone, Jie Shan, and Tony F. Heinz. Atomically thin  $\text{MoS}_2$ : A new direct-gap semiconductor. *Phys. Rev. Lett.*, 105:136805, Sep 2010.
- [24] Andrea Splendiani, Liang Sun, Yuanbo Zhang, Tianshu Li, Jonghwan Kim, Chi-Yung Chim, Giulia Galli, and Feng Wang. Emerging photoluminescence in monolayer  $\text{MoS}_2$ . *Nano Letters*, 10(4):1271–1275, Apr 2010.
- [25] Kin Fai Mak and Jie Shan. Photonics and optoelectronics of 2d semiconductor transition metal dichalcogenides. *Nature Photonics*, 10(4):216–226, Apr 2016.
- [26] Marco Bernardi, Maurizia Palummo, and Jeffrey C. Grossman. Extraordinary sunlight absorption and one nanometer thick photovoltaics using two-dimensional monolayer materials. *Nano Letters*, 13(8):3664–3670, Aug 2013.
- [27] Jun Dai and Xiao Cheng Zeng. Bilayer phosphorene: Effect of stacking order on bandgap and its potential applications in thin-film solar cells. *The Journal of Physical Chemistry Letters*, 5(7):1289–1293, Apr 2014.
- [28] Haidi Wang, Xingxing Li, Zhao Liu, and Jinlong Yang.  $\psi$ -phosphorene: a new allotrope of phosphorene. *Phys. Chem. Chem. Phys.*, 19:2402–2408, 2017.
- [29] Kai Wu, Huanhuan Ma, Yunzhi Gao, Wei Hu, and Jinlong Yang. Highly-efficient heterojunction solar cells based on two-dimensional tellurene and transition metal dichalcogenides. *J. Mater. Chem. A*, 7:7430–7436, 2019.
- [30] Youngjun Kim, Sangyoon Lee, Jeong-Gyu Song, Kyung Yong Ko, Whang Je Woo, Suk Woo Lee, Minwoo Park, Hoonkyung Lee, Zonghoon Lee, Hyunyoung Choi, et al. 2d transition metal dichalcogenide heterostructures for p-and n-type photovoltaic self-powered gas sensor. *Advanced Functional Materials*, 30(43):2003360, 2020.

- [31] Fei Chen, Lei Wang, Xiaohong Ji, and Qinyuan Zhang. Temperature-dependent two-dimensional transition metal dichalcogenide heterostructures: Controlled synthesis and their properties. *ACS Applied Materials & Interfaces*, 9(36):30821–30831, Sep 2017.
- [32] B. Amin, N. Singh, and U. Schwingenschlögl. Heterostructures of transition metal dichalcogenides. *Phys. Rev. B*, 92:075439, Aug 2015.
- [33] Frank Ceballos, Matthew Z. Bellus, Hsin-Ying Chiu, and Hui Zhao. Ultrafast charge separation and indirect exciton formation in a mos2–mose2 van der waals heterostructure. *ACS Nano*, 8(12):12717–12724, Dec 2014.
- [34] Georg Kresse and Jürgen Furthmüller. Efficiency of ab-initio total energy calculations for metals and semiconductors using a plane-wave basis set. *Comput. Mater. Sci.*, 6:15–50, 1996.
- [35] Georg Kresse and Jürgen Furthmüller. Efficient iterative schemes for ab initio total-energy calculations using a plane-wave basis set. *Phys. Rev. B*, 54:11169–11204, 1996.
- [36] Pierre Hohenberg and Walter Kohn. Inhomogeneous electron gas. *Phys. Rev.*, 136–143:B864, 1964.
- [37] Walter Kohn and Lu Jeu Sham. Self-consistent equations including exchange and correlation effects. *Phys. Rev.*, 140:A1133–A1138, 1965.
- [38] John P Perdew, Kieron Burke, and Matthias Ernzerhof. Generalized gradient approximation made simple. *Phys. Rev. Lett.*, 77:3865–3868, 1996.
- [39] Jochen Heyd, Gustavo E Scuseria, and Matthias Ernzerhof. Hybrid functionals based on a screened coulomb potential. *The Journal of chemical physics*, 118(18):8207–8215, 2003.
- [40] Jiří Klimeš, David R Bowler, and Angelos Michaelides. Chemical accuracy for the van der waals density functional. *Journal of Physics: Condensed Matter*, 22(2):022201, dec 2009.
- [41] Georg Kresse and Daniel Joubert. From ultrasoft pseudopotentials to the projector augmented-wave method. *Phys. Rev. B*, 59:1758–1775, 1999.
- [42] Peter E Blöchl. Projector augmented-wave method. *Phys. Rev. B*, 50:17953–17979, 1994.
- [43] Hendrik J Monkhorst and James D Pack. Special points for brillouin-zone integrations. *Phys. Rev. B*, 13:5188–5192, 1976.
- [44] M. Shishkin and G. Kresse. Implementation and performance of the frequency-dependent *gw* method within the paw framework. *Phys. Rev. B*, 74:035101, Jul 2006.
- [45] Arash A. Mostofi, Jonathan R. Yates, Young-Su Lee, Ivo Souza, David Vanderbilt, and Nicola Marzari. wannier90: A tool for obtaining maximally-localised wannier functions. *Computer*

- Physics Communications*, 178(9):685–699, 2008.
- [46] Houlong L. Zhuang and Richard G. Hennig. Single-layer group-iii monochalcogenide photocatalysts for water splitting. *Chemistry of Materials*, 25(15):3232–3238, Aug 2013.
  - [47] Maytal Caspary Toroker, Dalal K. Kanan, Nima Alidoust, Leah Y. Isseroff, Peilin Liao, and Emily A. Carter. First principles scheme to evaluate band edge positions in potential transition metal oxide photocatalysts and photoelectrodes. *Phys. Chem. Chem. Phys.*, 13:16644–16654, 2011.
  - [48] Stefan Albrecht, Lucia Reining, Rodolfo Del Sole, and Giovanni Onida. Ab initio calculation of excitonic effects in the optical spectra of semiconductors. *Phys. Rev. Lett.*, 80:4510–4513, May 1998.
  - [49] Michael Rohlfing and Steven G. Louie. Electron-hole excitations and optical spectra from first principles. *Phys. Rev. B*, 62:4927–4944, Aug 2000.
  - [50] J. C. Taylor. Tamm-dancoff method. *Phys. Rev.*, 95:1313–1317, Sep 1954.
  - [51] Ravinder Pawar and Akanksha Ashok Sangolkar. Density functional theory based hse06 calculations to probe the effects of defect on electronic properties of monolayer tmdcs. *Computational and Theoretical Chemistry*, 1205:113445, 2021.
  - [52] Nouridine Zibouche, Agnieszka Kuc, Janice Musfeldt, and Thomas Heine. Transition-metal dichalcogenides for spintronic applications. *Annalen der Physik*, 526(9-10):395–401, 2014.
  - [53] K. Kośmider and J. Fernández-Rossier. Electronic properties of the mos<sub>2</sub>-ws<sub>2</sub> heterojunction. *Phys. Rev. B*, 87:075451, Feb 2013.
  - [54] Chenxi Zhang, Cheng Gong, Yifan Nie, Kyung-Ah Min, Chaoping Liang, Young Jun Oh, Hengji Zhang, Weihua Wang, Suklyun Hong, Luigi Colombo, Robert M Wallace, and Kyeongjae Cho. Systematic study of electronic structure and band alignment of monolayer transition metal dichalcogenides in van der waals heterostructures. *2D Materials*, 4(1):015026, nov 2016.
  - [55] William Shockley. The shockley-queisser limit. *J. Appl. Phys*, 32(3):510–519, 1961.
  - [56] Henan Li, Jing-Kai Huang, Yumeng Shi, and Lain-Jong Li. Toward the growth of high mobility 2d transition metal dichalcogenide semiconductors. *Advanced Materials Interfaces*, 6(24):1900220, 2019.
  - [57] Wenxu Zhang, Zhishuo Huang, Wanli Zhang, and Yanrong Li. Two-dimensional semiconductors with possible high room temperature mobility. *Nano Research*, 7(12), Dec 2014.

- [58] Changgu Lee, Hugen Yan, Louis E. Brus, Tony F. Heinz, James Hone, and Sunmin Ryu. Anomalous lattice vibrations of single- and few-layer mos<sub>2</sub>. *ACS Nano*, 4(5):2695–2700, May 2010.
- [59] Humberto R. Gutiérrez, Nestor Perea-López, Ana Laura Elías, Ayse Berkdemir, Bei Wang, Ruitao Lv, Florentino López-Urías, Vincent H. Crespi, Humberto Terrones, and Mauricio Terrones. Extraordinary room-temperature photoluminescence in triangular ws<sub>2</sub> monolayers. *Nano Letters*, 13(8):3447–3454, Aug 2013.
- [60] Weijie Zhao, Zohreh Ghorannevis, Leiqiang Chu, Minglin Toh, Christian Kloc, Ping-Heng Tan, and Goki Eda. Evolution of electronic structure in atomically thin sheets of ws<sub>2</sub> and wse<sub>2</sub>. *ACS Nano*, 7(1):791–797, Jan 2013.
- [61] Yi Zhang, Tay-Rong Chang, Bo Zhou, Yong-Tao Cui, Hao Yan, Zhongkai Liu, Felix Schmitt, James Lee, Rob Moore, Yulin Chen, Hsin Lin, Horng-Tay Jeng, Sung-Kwan Mo, Zahid Hussain, Arun Bansil, and Zhi-Xun Shen. Direct observation of the transition from indirect to direct bandgap in atomically thin epitaxial mose<sub>2</sub>. *Nature Nanotechnology*, 9(2):111–115, Feb 2014.
- [62] Charlotte Herbig, Canxun Zhang, Fauzia Mujid, Saien Xie, Zahra Pedramrazi, Jiwoong Park, and Michael F. Crommie. Local electronic properties of coherent single-layer ws<sub>2</sub>/wse<sub>2</sub> lateral heterostructures. *Nano Letters*, 21(6):2363–2369, Mar 2021.
- [63] Alejandro Molina-Sánchez, Davide Sangalli, Kerstin Hummer, Andrea Marini, and Ludger Wirtz. Effect of spin-orbit interaction on the optical spectra of single-layer, double-layer, and bulk mos<sub>2</sub>. *Phys. Rev. B*, 88:045412, Jul 2013.
- [64] Engin Torun, Henrique P. C. Miranda, Alejandro Molina-Sánchez, and Ludger Wirtz. Interlayer and intralayer excitons in mos<sub>2</sub>/ws<sub>2</sub> and mose<sub>2</sub>/wse<sub>2</sub> heterobilayers. *Phys. Rev. B*, 97:245427, Jun 2018.
- [65] Timothy C. Berkelbach, Mark S. Hybertsen, and David R. Reichman. Theory of neutral and charged excitons in monolayer transition metal dichalcogenides. *Phys. Rev. B*, 88:045318, Jul 2013.
- [66] A. R. Klots, A. K. M. Newaz, Bin Wang, D. Prasai, H. Krzyzanowska, Junhao Lin, D. Caudel, N. J. Ghimire, J. Yan, B. L. Ivanov, K. A. Velizhanin, A. Burger, D. G. Mandrus, N. H. Tolk, S. T. Pantelides, and K. I. Bolotin. Probing excitonic states in suspended two-dimensional semiconductors by photocurrent spectroscopy. *Scientific Reports*, 4(1):6608, Oct 2014.

- [67] Alexey Chernikov, Timothy C. Berkelbach, Heather M. Hill, Albert Rigosi, Yilei Li, Burak Aslan, David R. Reichman, Mark S. Hybertsen, and Tony F. Heinz. Exciton binding energy and nonhydrogenic rydberg series in monolayer  $\text{ws}_2$ . *Phys. Rev. Lett.*, 113:076802, Aug 2014.
- [68] Xiaoli Ma, Shaohua Fu, Jianwei Ding, Meng Liu, Ang Bian, Fang Hong, Jiatao Sun, Xiaoxian Zhang, Xiaohui Yu, and Dawei He. Robust interlayer exciton in  $\text{ws}_2/\text{mose}_2$  van der waals heterostructure under high pressure. *Nano Letters*, 21(19):8035–8042, Oct 2021.
- [69] Jed Kistner-Morris, Ao Shi, Erfu Liu, Trevor Arp, Farima Farahmand, Takashi Taniguchi, Kenji Watanabe, Vivek Aji, Chun Hung Lui, and Nathaniel Gabor. Electric-field tunable type-i to type-ii band alignment transition in  $\text{mose}_2/\text{ws}_2$  heterobilayers. *Nature Communications*, 15(1):4075, May 2024.
- [70] Hannu-Pekka Komsa and Arkady V. Krasheninnikov. Electronic structures and optical properties of realistic transition metal dichalcogenide heterostructures from first principles. *Phys. Rev. B*, 88:085318, Aug 2013.
- [71] G. Kresse and J. Hafner. Ab initio molecular-dynamics simulation of the liquid-metal–amorphous-semiconductor transition in germanium. *Phys. Rev. B*, 49:14251–14269, May 1994.
- [72] Shuichi Nosé. A unified formulation of the constant temperature molecular dynamics methods. *The Journal of chemical physics*, 81(1):511–519, 1984.
- [73] Liangbo Liang and Vincent Meunier. First-principles raman spectra of  $\text{mos}_2$ ,  $\text{ws}_2$  and their heterostructures. *Nanoscale*, 6:5394–5401, 2014.
- [74] Bin Amin, Thaneshwor P. Kaloni, Georg Schreckenbach, and Michael S. Freund. Materials properties of out-of-plane heterostructures of  $\text{MoS}_2\text{-WSe}_2$  and  $\text{WS}_2\text{-MoSe}_2$ . *Applied Physics Letters*, 108(6):063105, 02 2016.
- [75] Xiaohui Hu, Liangzhi Kou, and Litao Sun. Stacking orders induced direct band gap in bilayer  $\text{mose}_2\text{-wse}_2$  lateral heterostructures. *Scientific Reports*, 6(1):31122, Aug 2016.
- [76] Fang Wang, Junyong Wang, Shuang Guo, Jinzhong Zhang, Zhigao Hu, and Junhao Chu. Tuning coupling behavior of stacked heterostructures based on  $\text{mos}_2$ ,  $\text{ws}_2$ , and  $\text{wse}_2$ . *Scientific Reports*, 7(1):44712, Mar 2017.
- [77] Anna Krivosheeva, Victor Shaposhnikov, Victor Borisenko, and Jean-Louis Lazzari. Energy band gap tuning in te-doped  $\text{ws}_2/\text{wse}_2$  heterostructures. *Journal of Materials Science*, 55(23):9695–9702, Aug 2020.

- [78] Humberto Terrones, Florentino López-Urías, and Mauricio Terrones. Novel hetero-layered materials with tunable direct band gaps by sandwiching different metal disulfides and diselenides. *Scientific Reports*, 3(1):1549, Mar 2013.
- [79] See Supplemental material at [ ] for the HSE06 &  $G_0W_0$  band structures, reported carrier mobilities, BSE optical absorption plots, and effective masses of the monolayers, and AIMD simulation plots, orbital projected PBE band structures, and electrostatic potential energy plots of the heterostructures. It also contains the intermediate solar cell parameters required for the calculation of power conversion efficiencies of the heterostructures.
- [80] Markus C Scharber, David Mühlbacher, Markus Koppe, Patrick Denk, Christoph Waldauf, Alan J Heeger, and Christoph J Brabec. Design rules for donors in bulk-heterojunction solar cells – towards 10% energy-conversion efficiency. *Advanced materials*, 18(6):789–794, 2006.
- [81] Hongyan Guo, Ning Lu, Jun Dai, Xiaojun Wu, and Xiao Cheng Zeng. Phosphorene nanoribbons, phosphorus nanotubes, and van der waals multilayers. *The Journal of Physical Chemistry C*, 118(25):14051–14059, Jun 2014.
- [82] Yan Liang, Ying Dai, Yandong Ma, Lin Ju, Wei Wei, and Baibiao Huang. Novel titanium nitride halide tin<sub>x</sub> (x = f, cl, br) monolayers: potential materials for highly efficient excitonic solar cells. *J. Mater. Chem. A*, 6:2073–2080, 2018.
- [83] Ming-Yang Li, Chang-Hsiao Chen, Yumeng Shi, and Lain-Jong Li. Heterostructures based on two-dimensional layered materials and their potential applications. *Materials Today*, 19(6):322–335, 2016.
- [84] Marco M. Furchi, Andreas Pospischil, Florian Libisch, Joachim Burgdörfer, and Thomas Mueller. Photovoltaic effect in an electrically tunable van der waals heterojunction. *Nano Letters*, 14(8):4785–4791, Aug 2014.
- [85] Yongji Gong, Sidong Lei, Gonglan Ye, Bo Li, Yongmin He, Kuntal Keyshar, Xiang Zhang, Qizhong Wang, Jun Lou, Zheng Liu, Robert Vajtai, Wu Zhou, and Pulickel M. Ajayan. Two-step growth of two-dimensional wse<sub>2</sub>/mose<sub>2</sub> heterostructures. *Nano Letters*, 15(9):6135–6141, Sep 2015.
- [86] Marco Bernardi, Maurizia Palummo, and Jeffrey C. Grossman. Semiconducting monolayer materials as a tunable platform for excitonic solar cells. *ACS Nano*, 6(11):10082–10089, Nov 2012.

- [87] Yuliang Mao, Chuangqing Qin, Jing Wang, and Jianmei Yuan. A two-dimensional  $\alpha$ -as/ $\alpha$ -asp van der waals heterostructure for photovoltaic applications. *Phys. Chem. Chem. Phys.*, 24:16058–16064, 2022.
- [88] Xiaoqiang Li, Wenchao Chen, Shengjiao Zhang, Zhiqian Wu, Peng Wang, Zhijuan Xu, Hongsheng Chen, Wenyan Yin, Huikai Zhong, and Shisheng Lin. 18.5 % efficient graphene/gaas van der waals heterostructure solar cell. *Nano Energy*, 16:310–319, 2015.
- [89] Michael Grätzel. Photoelectrochemical cells. *Nature*, 414(6861):338–344, Nov 2001.
- [90] Yunguo Li, Yan-Ling Li, Carlos Moyses Araujo, Wei Luo, and Rajeev Ahuja. Single-layer mos2 as an efficient photocatalyst. *Catal. Sci. Technol.*, 3:2214–2220, 2013.



# Supplemental Material for 2D Transition-metal dichalcogenides based bilayer heterojunctions for efficient solar cells and photocatalytic applications

Khushboo Dange,<sup>\*</sup> Rachana Yogi,<sup>†</sup> and Alok Shukla<sup>‡</sup>

*Department of Physics, Indian Institute of Technology Bombay, Powai, Mumbai 400076, India*

## A. TMD Monolayers

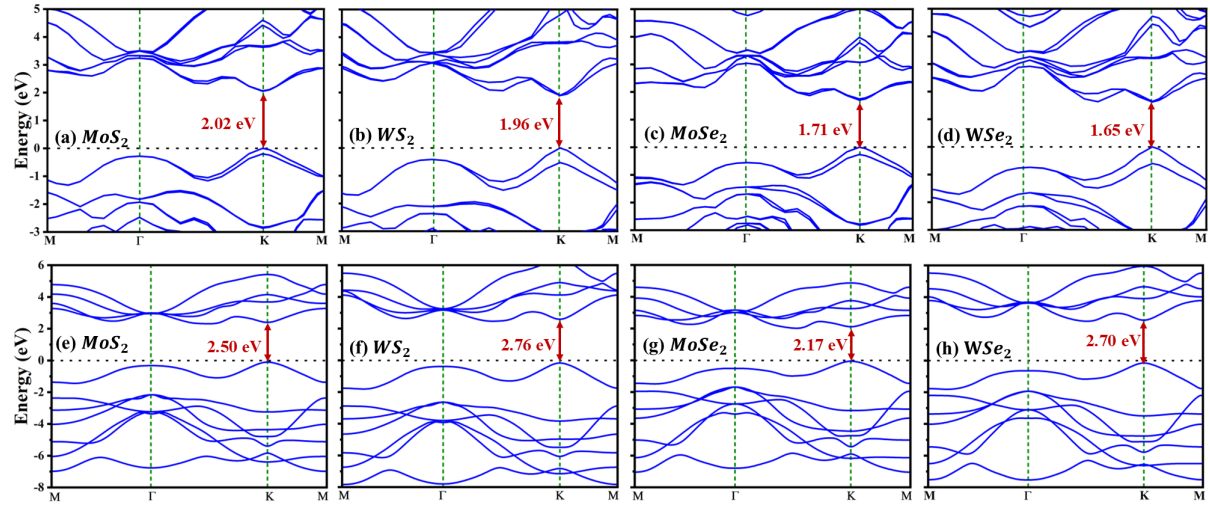


Figure S1. Band structures of the considered TMD monolayers, calculated using (a)-(d) HSE06 functional and (e)-(f)  $G_0W_0$  approximation.

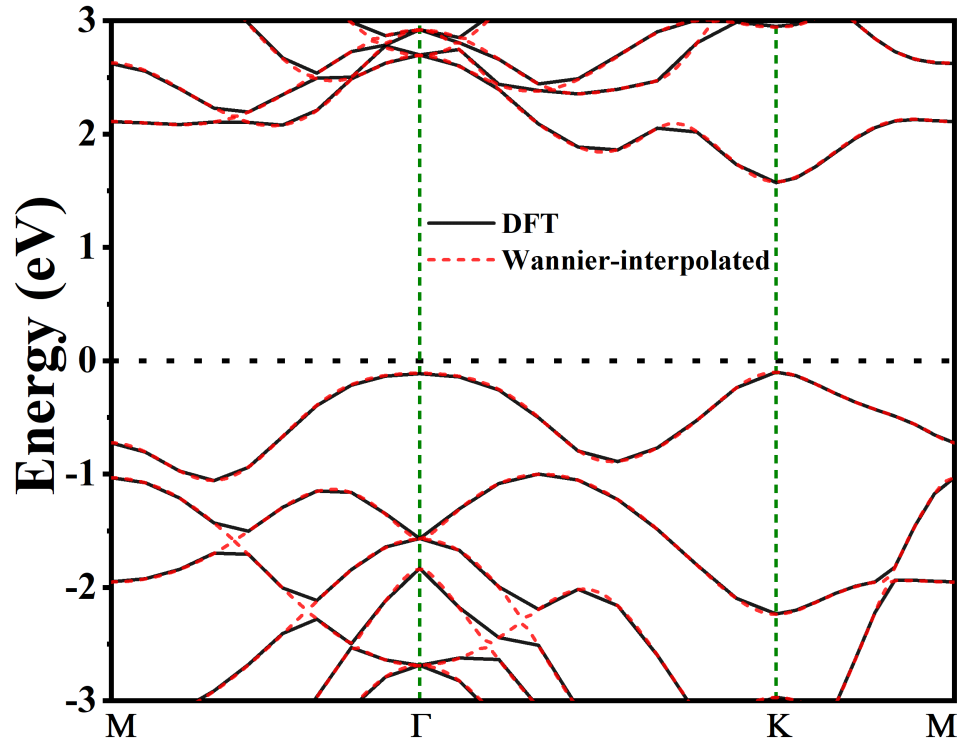
<sup>\*</sup> khushboodange@gmail.com

<sup>†</sup> yogirachana04@gmail.com

<sup>‡</sup> shukla@iitb.ac.in

Table S1. Reported carrier mobilities ( $\mu$ ) of the 2D TMDs under consideration

2D TMDs $\mu$ ( $10^3 \text{cm}^3 \text{V}^{-1} \text{S}^{-1}$ ) References		
MoS <sub>2</sub>	0.410	[1]
MoSe <sub>2</sub>	0.240	[2]
WS <sub>2</sub>	1.102	[1]
WSe <sub>2</sub>	0.705	[1]

Figure S2. GGA-PBE (without SOC) band structure of the MoS<sub>2</sub> monolayer.

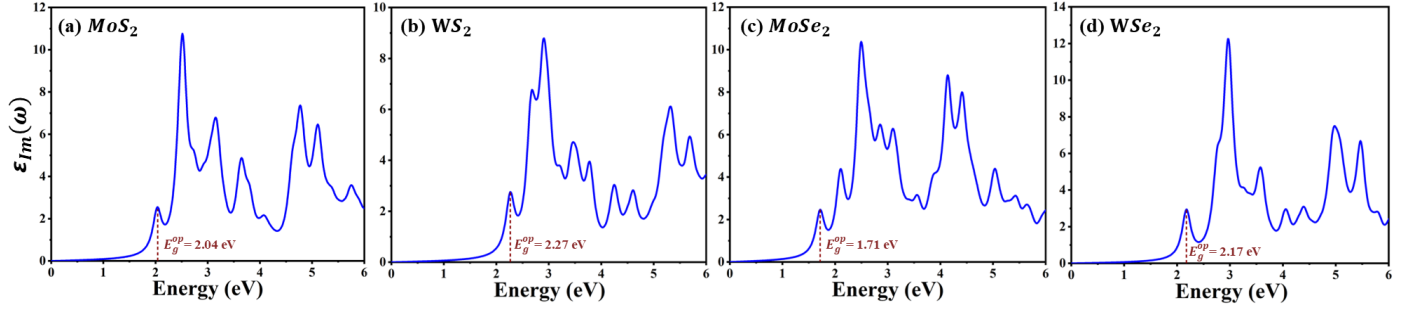


Figure S3. Imaginary part of dielectric function,  $\epsilon_{Im}(\omega)$  as a function of energy of the incident photon for the considered monolayers using BSE.

Table S2. Calculated effective masses of the electrons ( $m_e^*$ ) and holes ( $m_h^*$ ) in terms of free electron mass ( $m_0$ ) for the considered TMD monolayers.

Monolayers	$m_e^*(m_0)$		$m_h^*(m_0)$	
	(K $\rightarrow$ $\Gamma$ )	(K $\rightarrow$ M)	(K $\rightarrow$ $\Gamma$ )	(K $\rightarrow$ M)
MoS <sub>2</sub>	0.48	0.54	0.56	0.70
WS <sub>2</sub>	0.32	0.34	0.42	0.49
MoSe <sub>2</sub>	0.55	0.63	0.63	0.79
WSe <sub>2</sub>	0.35	0.39	0.45	0.53

## B. TMD heterostructures

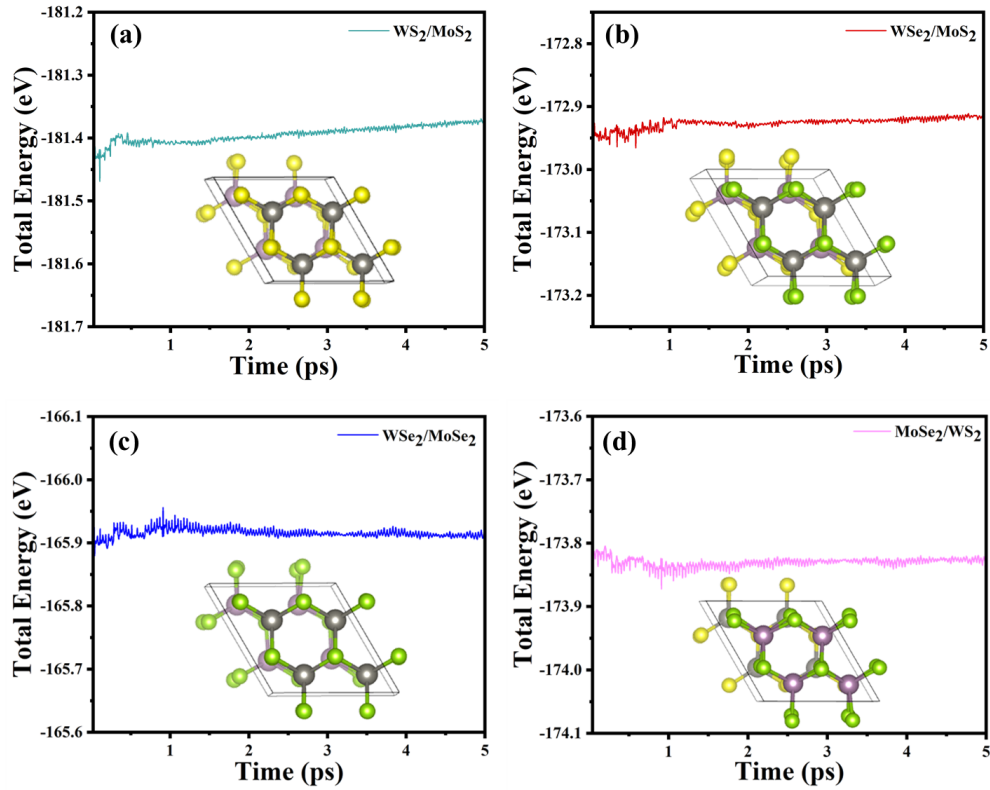


Figure S4. Total energy as a function of time steps for (a)  $\text{WS}_2/\text{MoS}_2$ , (b)  $\text{WSe}_2/\text{MoS}_2$ , (c)  $\text{WSe}_2/\text{MoSe}_2$ , and (d)  $\text{MoSe}_2/\text{WS}_2$  systems, obtained from the AIMD simulations at 500K. The final structures obtained at the end of simulations are also shown in the inset. Here, purple, grey, yellow, and green spheres represent the Mo, W, S, and Se atoms, respectively.

Table S3.  $E_g^{QP}$  values using 200 unoccupied bands in  $G_0W_0$  calculations

S.No.	Heterostructures	$E_g^{QP}$ (eV)
1	WS <sub>2</sub> /MoS <sub>2</sub>	2.13
2	MoSe <sub>2</sub> /MoS <sub>2</sub>	1.92
3	MoSe <sub>2</sub> /WS <sub>2</sub>	1.93
4	WSe <sub>2</sub> /MoS <sub>2</sub>	2.07
5	WSe <sub>2</sub> /MoSe <sub>2</sub>	1.98
6	WSe <sub>2</sub> /WS <sub>2</sub>	2.14

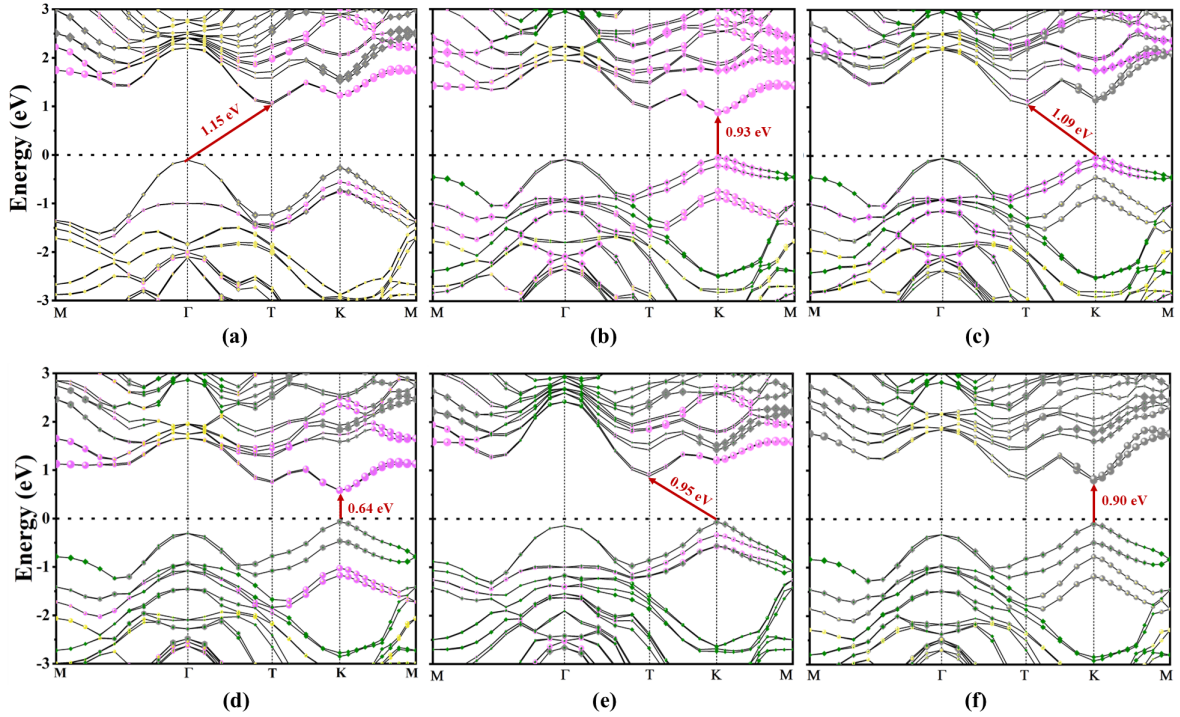


Figure S5. Projected band structures of (a) WS<sub>2</sub>/MoS<sub>2</sub>, (b) MoSe<sub>2</sub>/MoS<sub>2</sub>, (c) MoSe<sub>2</sub>/WS<sub>2</sub>, (d) WSe<sub>2</sub>/MoS<sub>2</sub>, (e) WSe<sub>2</sub>/MoSe<sub>2</sub> and (f) WSe<sub>2</sub>/WS<sub>2</sub> heterojunctions using PBE functional. Pink, grey, yellow, and green spheres (diamonds) denote the Mo, W, S, and Se atoms of the acceptor (donor) semiconductors.

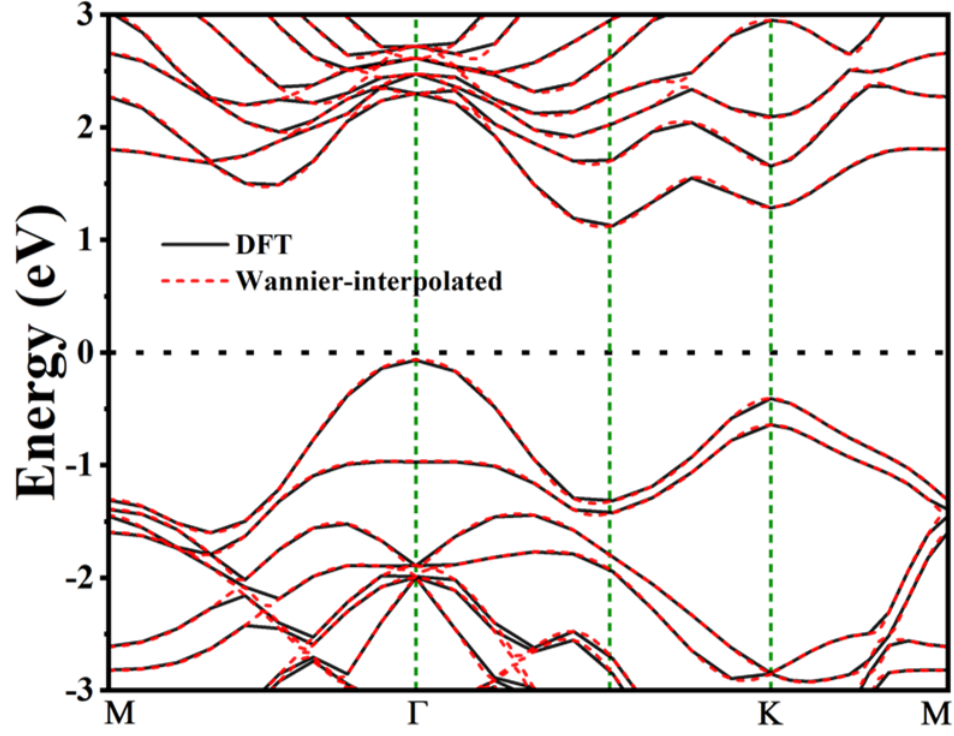


Figure S6. GGA-PBE band structure (without SOC) of the WS<sub>2</sub>/MoS<sub>2</sub> heterostructure.

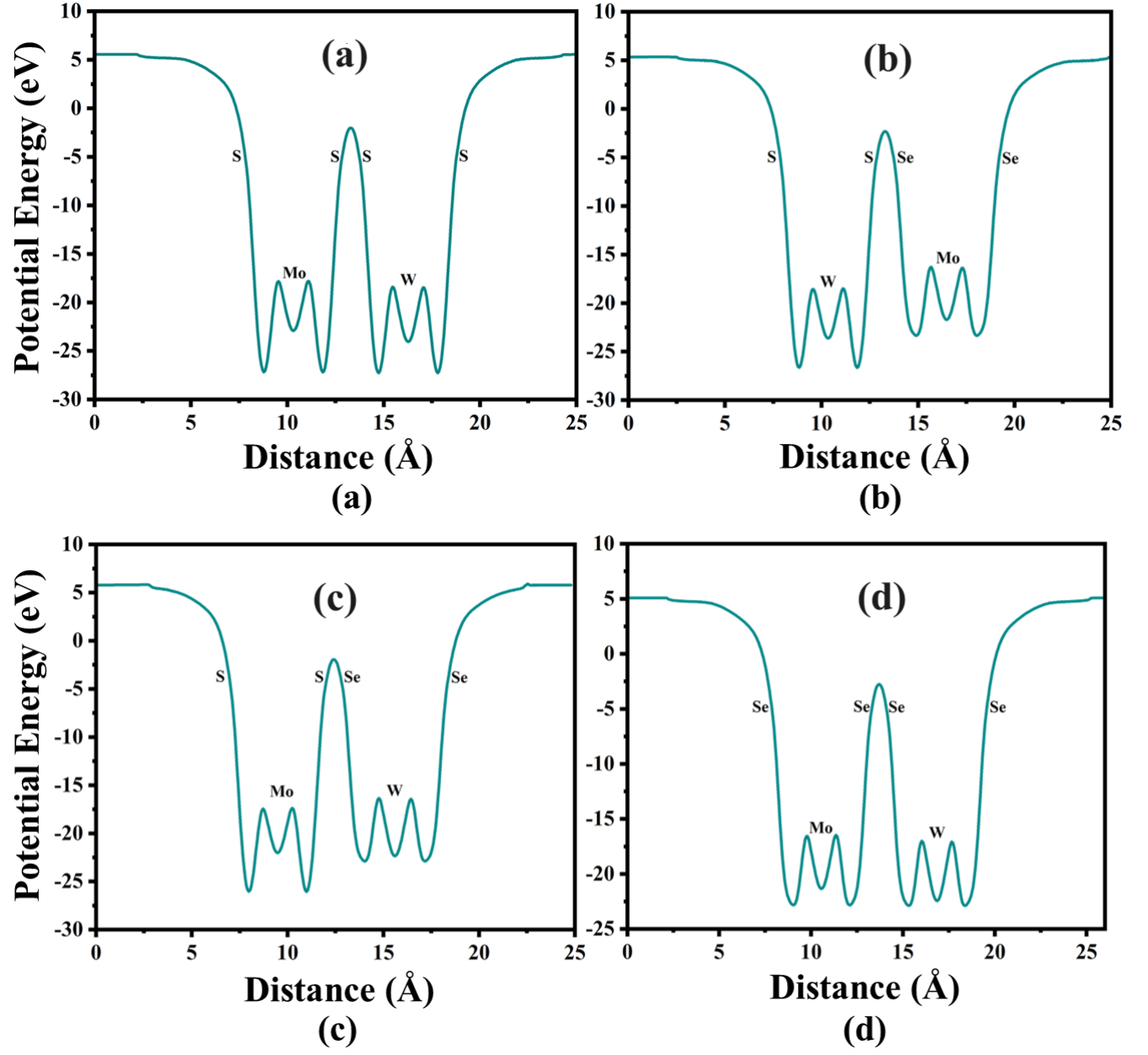


Figure S7. Electrostatic potential energy as a function of distance along the  $z$ -direction for (a)  $\text{WS}_2/\text{MoS}_2$ , (b)  $\text{MoSe}_2/\text{WS}_2$ , (c)  $\text{WSe}_2/\text{MoS}_2$ , and (d)  $\text{WSe}_2/\text{MoSe}_2$  heterojunctions.

Table S4. Solar cell parameters, donor band gap ( $E_g^d$ ), conduction band offset ( $\Delta E_c$ ), open circuit voltage ( $V_{oc}$ ), and current density ( $J_{sc}$ ), of the heterostructures under consideration calculated at DFT level using HSE06 functional.

S.No.	Heterostructures	$E_g^d$ (eV)	$\Delta E_c$ (eV)	$V_{oc}$ (V)	$J_{sc}$ (mA/cm <sup>2</sup> )
1	WS <sub>2</sub> /MoS <sub>2</sub>	1.96	0.37	1.28	15.48
2	MoSe <sub>2</sub> /MoS <sub>2</sub>	1.71	0.12	1.29	22.16
3	MoSe <sub>2</sub> /WS <sub>2</sub>	1.71	0.17	1.23	22.16
4	WSe <sub>2</sub> /MoS <sub>2</sub>	1.65	0.43	0.92	23.98
5	WSe <sub>2</sub> /MoSe <sub>2</sub>	1.65	0.31	1.04	23.98
6	WSe <sub>2</sub> /WS <sub>2</sub>	1.65	0.11	1.24	23.98

Table S5. Solar cell parameters, donor band gap ( $E_g^d$ ), conduction band offset ( $\Delta E_c$ ), open circuit voltage ( $V_{oc}$ ), and current density ( $J_{sc}$ ), of the heterostructures under consideration calculated at G<sub>0</sub>W<sub>0</sub> level.

S.No.	Heterostructures	$E_g^d$ (eV)	$\Delta E_c$ (eV)	$V_{oc}$ (V)	$J_{sc}$ (mA/cm <sup>2</sup> )
1	WS <sub>2</sub> /MoS <sub>2</sub>	2.27	0.43	1.54	9.39
2	MoSe <sub>2</sub> /MoS <sub>2</sub>	1.71	0.38	1.03	22.16
3	WSe <sub>2</sub> /MoS <sub>2</sub>	2.17	0.96	0.91	11.10
4	WSe <sub>2</sub> /MoSe <sub>2</sub>	2.17	0.58	1.29	11.10
5	WSe <sub>2</sub> /WS <sub>2</sub>	2.17	0.53	1.34	11.10



Table S6. Solar cell parameters, donor band gap ( $E_g^d$ ), conduction band offset ( $\Delta E_c$ ), open circuit voltage ( $V_{oc}$ ), and current density ( $J_{sc}$ ), of the heterostructures under consideration calculated at  $G_0W_0 + \text{SOC}$  level.

S.No.	Heterostructures	$E_g^d$ (eV)	$\Delta E_c$ (eV)	$V_{oc}$ (V)	$J_{sc}$ (mA/cm <sup>2</sup> )
1	WS <sub>2</sub> /MoS <sub>2</sub>	2.01	0.39	1.32	14.34
2	MoSe <sub>2</sub> /MoS <sub>2</sub>	1.60	0.38	0.92	25.44
3	WSe <sub>2</sub> /MoS <sub>2</sub>	1.87	0.92	0.65	17.68
4	WSe <sub>2</sub> /MoSe <sub>2</sub>	1.87	0.54	1.03	17.68
5	WSe <sub>2</sub> /WS <sub>2</sub>	1.87	0.53	1.04	17.68

- 
- [1] Henan Li, Jing-Kai Huang, Yumeng Shi, and Lain-Jong Li. Toward the growth of high mobility 2D transition metal dichalcogenide semiconductors. *Advanced Materials Interfaces*, 6(24), 2019.
- [2] Wenxu Zhang, Zhishuo Huang, Wanli Zhang, and Yanrong Li. Two-dimensional semiconductors with possible high room temperature mobility. *Nano Research*, 7(12), 2014.